STRUCTURALLY INTEGRATED ANTENNAS ON A JOINED-WING AIRCRAFT

THESIS

Ben P. Smallwood, Captain, USAF

AFIT/GAE/ENY/03-7

DEPARTMENT OF THE AIR FORCE
AIR UNIVERSITY

AIR FORCE INSTITUTE OF TECHNOLOGY

Wright-Patterson Air Force Base, Ohio

The views expressed in this thesis are those of the author and do not reflect the official policy or position of the United States Air Force, Department of Defense, or the United States Government.

AFIT/GAE/ENY/03-7

STRUCTURALLY INTEGRATED ANTENNAS ON A JOINED-WING AIRCRAFT

THESIS

Presented to the Faculty
Department of Aeronautics and Astronautics
Graduate School of Engineering and Management
Air Force Institute of Technology
Air University
Air Education and Training Command
in Partial Fulfillment of the Requirements for the
Degree of Master of Science in Aeronautical Engineering

Ben P. Smallwood, B.S.
Captain, USAF

March 2003

AFIT/GAE/ENY/03-7

STRUCTURALLY INTEGRATED ANTENNAS ON A JOINED-WING AIRCRAFT

Ben P. Smallwood, B.S.

Captain, USAF

Approved:

LtCol Robert A. Canfield (Chairman)	Date
Andrew J. Terzuoli (Co-Chairman)	Date
Curtis H. Spenny (Committee Member)	Date

Acknowledgements

I would like to express my appreciation to my thesis advisors, LtCol Robert Canfield and Dr. Andrew Terzuoli, for their guidance and instruction throughout this thesis effort. Their insight, experience, direction and enthusiasm were greatly valued.

I would like to thank Dr. Gary Thiele for taking the time to answer questions, review my work, and share his knowledge of antenna theory, and also Jeremiah Allen for the many hours of programming to generate data that I needed for my research.

Finally, I would like to recognize my family. I could not have completed this endeavor without the support and encouragement of my wife. I am continuously amazed at her ability to adapt to all that life brings her way. I am also thankful for my two beautiful children. No matter what was going on at school, they could always bring a smile to my face.

Ben P. Smallwood

Table of Contents

List of Figures

List of Tables

AFIT/GAE/ENY/03-7

Abstract

This research is a foundational study of conformal, load-bearing antenna arrays embedded into the wing structure of a joined-wing aircraft. It is a multidisciplinary effort that touches on the aerodynamic, structural, and electromagnetic design considerations that stem from this unique type of sensor integration. The antenna performance, Finite Element Model (FEM), and control surface effectiveness are investigated. The theory describing an ensemble of dipole antenna elements that conform to the shape of a section of the joined wing is developed. The far field, free space radiation pattern of the sensor is then analyzed for a wing that is deflected due to typical aerodynamic loading. This pattern is compared to the same antenna when the wing is not deformed. A FEM of the antenna elements is created and incorporated into the full FEM of the joined-wing aircraft allowing its structural impact to be realized. Based on the positioning of these large sensor arrays, control surfaces are placed and examined to achieve the proper handling capabilities necessary for this type of aircraft.

The results of this study show that wing deflections due to typical aerodynamic loads produce significant disturbances to the radiation pattern of a conformal antenna when end-fire phasing is applied. Active compensation for wing deformation will have to be applied to correct the beam steering. The basic array theory provides a useful tool for analyzing the radiation pattern of an array that conforms to the surface of an undeformed wing. On wings deformed due to typical aerodynamic loads, the main beam elevation pointing angle varies considerably between the basic array theory and NEC-Win Plus+^{TM} solutions. Also, the reversal speed of an outboard aileron is determined.

STRUCTURALLY INTEGRATED ANTENNAS ON A JOINED-WING AIRCRAFT

I. Introduction

This research effort focused on load-bearing, conformal antennas embedded into the skin of a joined-wing type of aircraft. It was part of the ongoing work described in [2]. One of the main areas of interest was determining the pointing accuracy of the antenna array as the wing was deflected due to typical aerodynamic loads acting on the lifting surfaces.

A simplified, composite FEM of Northrop Grumman's Sensorcraft - Conformal Load Bearing Antenna Structure [15] (S-CLAS) was created. This new element was then substituted into the joined-wing model in place of the elements on each wing surface where the antenna arrays will be located.

Placement of the antennas is an important issue when designing the aircraft due to the fact that the conformal antennas utilize the entire chord of the wing. Therefore, control surfaces cannot be placed in any spanwise section of the wings where the antennas are located. The size of the antennas is performance driven, but there are size limitations based on the amount of control surfaces needed to effectively turn and trim the joined-wing aircraft. Thus, the control surface effectiveness is another area of interest.

1.1 Background

Unmanned Arial Vehicles (UAVs) have become an integral part of the aeronautical engineer's vocabulary. These aircraft give the ability to maintain constant surveillance of ground activities. The notional sensorcraft is a UAV concept in which the Air Force Research Laboratory (AFRL) is fusing many of its state-of-the-art

technologies into a single aircraft [2]. The AFRL concept uses a joined front and aft wing and conformal antennas integrated into the wing structure. The wings connect in a diamond pattern when viewed from the front and from above as shown in Figure 1.1 [2]. This diamond shape allows the sensorcraft to view 360^o of its environment in the azimuth plane, thus allowing fewer potential targets to go undetected.

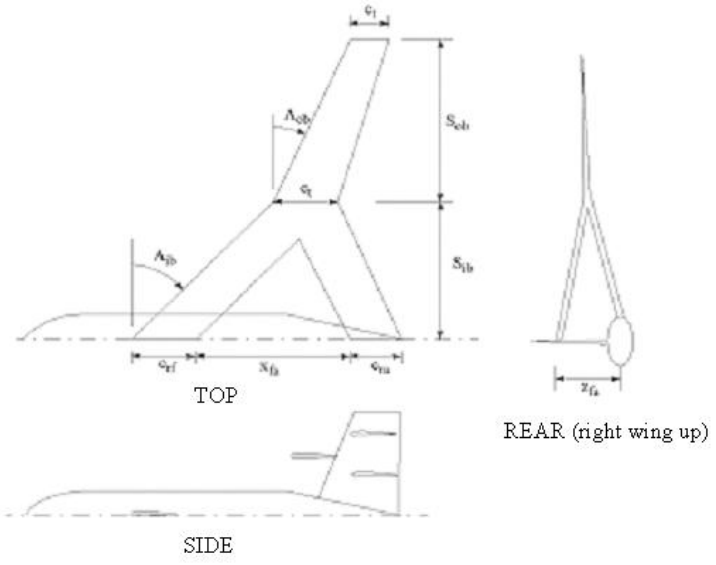

Figure 1.1 Joined-Wing Configuration

Table 1.1 [2] shows the geometric parameters of the current configuration. One can see that this aircraft has a very long tip-to-tip wingspan of approximately 64.5 meters (212 ft). A span of this magnitude makes the structure quite flexible, and this is a concern due to the embedded antennas. This type of design is not optimal when you are trying to keep a radar beam focused on a target. The amount of wing flexing allowed by the sensors tends to drive the structure to be stiffer. The sensors are discussed in more detail later in this section. An overview of the structural aspects of the joined-wing is first presented.

Many joined-wing designs have been studied over the past 17 years. The first joined-wing study was presented at a conference by J. Wolkovitch [25] in 1985. Livne presented an extensive survey of papers stemming from Wolkovitch's work and oth-

Table 1.1 Baseline Configuration Parameters

DESCRIPTION	LABEL	VALUE
Inboard Span	S_{ib}	26.00 m
Outboard Span	S_{ob}	6.25 m
Forward Root Chord	c_{rf}	2.50 m
Aft Root Chord	c_{ra}	2.50 m
Mid-Chord	c_m	2.50 m
Tip Chord	c_t	2.50 m
Forward-aft-x-offset	x_{fa}	22.00 m
Forward-aft-z-offset	z_{fa}	7.00 m
Inboard Sweep	Λ_{ib}	30 deg
Outboard Sweep	Λ_{ob}	30 deg
Airfoil		LRN-1015
Calculated Planform Area	S	145.0 m^2
Calculated Wing Volume		52.2 m^3

ers up to the year 2001 [7]. This survey is a valuable document for anyone doing research in any area of joined-wing design. One pertinent statement in his paper was the fact that antenna/lifting surface interactions should be studied. No past work accomplished in this area was referenced. G. Reich et. al. presented their work [17], which minimized deformation in the antenna by utilizing Active Aeroelastic Wing technology, but evaluating the antenna performance under these conditions was not the focus of their research. They did not model the antennas in this study as load-bearing parts of the structure, and therefore no stiffness properties were included for the antennas.

A conformal array type of antenna is necessary to allow the antennas to be embedded into the wing structure while maintaining a thin, efficient wing. The array then becomes a load-bearing member. In the present study the array is used in an end-fire configuration, with the main beam pointing normal to the leading edge of the wing. Proper phasing of the antenna elements in the array allows the beam to be steered in a plane extending off the end of the array. R. Mailloux [9] explains that conformal arrays may be treated as planar arrays if the length of the array is much less than the radius of curvature of the surface. Although this would make

the problem much simpler and might be relevant for a static scenario, the arrays in this case should be modeled as non-planar because the interest is in determining the disturbance caused by wing deformations. In this dynamic environment the orientation of the array elements will be constantly changing due to aerodynamic effects on the flexible wing, thus changing the pointing direction of each element in the array. Therefore, modeling the antenna as a conformal array right from the beginning is the best approach. Some simplifying assumptions about the interactions between elements and the array geometry are necessary in order to maintain the scope of this research and adapt planar array theory concepts [1, 21] to this particular conformal array. These tradeoffs must be examined so that a solution is obtained that is a realistic approximation.

Much of the textbook literature about arrays [1, 9, 21] focuses primarily on linear arrays. The basic concepts from linear array theory are then used to construct planar arrays. W. Kummer [5] comments that a planar array is essentially a string of linear arrays placed next to each other forming a two dimensional array. Due to the complexity of conformal arrays, many of the current textbooks focus on conformal arrays that span the circumference of a cylinder. Although the geometry of a cylindrical array is somewhat simple, even this case requires complex phasing of each element in the array in order to get proper beam shaping. When one transitions to conformal arrays, where each element may be pointing in a different direction, beam forming and beam steering become a complicated phasing issue.

When defining the antenna, there are typically two approaches. If the dimensions of the array (i.e. the number of elements and elemental spacing or the length of the array) are set as requirements, then the beamwidth and directivity are derived. Otherwise, the requirements are placed on the beamwidth and directivity. Balanis' textbook [1] gives a graphical representation of how the half-power beamwidth (a typical measurement for describing beamwidth) varies with the length of the array, which is measured in terms of wavelengths. In the initial effort of the research the

dimensions of the array were specified at approximately five feet in the chordwise direction and 42 feet spanwise.

1.2 Problem Statement

A conformal load-bearing antenna is a new concept in the sensor community. This type of antenna replaces the skin material on portions of the wings and therefore carries the aerodynamic loads that the skin would normally experience. As the wings deform due to typical flight conditions, the antenna is also bending and twisting away from its initial configuration. There are currently no methods that quantify the effects of this deformation on the conformal antenna performance, such as the changes in the main acquisition beam's magnitude and direction. A method should be developed that quickly and accurately measures the changes in these parameters.

1.3 Research Objectives

The goal of this research was to quantify the effect that wing deformation has on the pointing accuracy of conformal load-bearing antennas on a joined-wing aircraft. Three objectives were accomplished:

1. A finite element model of the conformal was developed and incorporated into the full aircraft FEM.
2. A theoretical antenna modeling approach for this antenna configuration was developed to quantify the change in antenna performance due to deformations. This approach was verified using a commercially available Method of Moments software package.
3. The control surface effectiveness was determined given the size and location of the antenna arrays.

1.4 Methodology

In an effort to control the scope of this research, an array of horizontally polarized, half-wavelength dipoles were used in the antenna analysis to model the actual conformal load-bearing antenna element. This allowed the basic theory of the antenna ensemble to be developed and verified. A MATLAB [10] code was developed to plot the radiation pattern of the array based on the location and orientation of each antenna element. A commercial software package, NEC-Win Plus+^{TM} [14], was then used to verify the analytical model. This software package utilizes the Method of Moments solution technique to analyze the antenna and determine its radiation pattern. Figure 1.2, created in NEC-Win Plus+^{TM}, shows one chordwise array of dipoles conforming to the shape of the airfoil.

Figure 1.2 One chordwise array of dipoles

The proposed antennas for the sensorcraft are conformal arrays that are integrated into the skin of the fore and aft wings. The antennas and inboard control surfaces are confined in the spanwise direction to fit between the fuselage and the wing joint. The amount of wing space available for the antennas will drive the pointing accuracy of the main beam, the maximum beam coverage area, and ultimately, the ability to find and track targets.

A simple model of the sensors was generated to incorporate the different layers of materials that make up the antenna's structure. This allowed a more accurate model of the wing structure to be generated. This also affects the overall stiffness of the structure, which in turn affects the amount of deflection in the wing. The

simplified model consisted of an electromagnetically transparent material called Astroquartz, honeycomb core material, and graphite epoxy, which acts as the main load-bearing component of the antenna element. This element model replaces the current aluminum elements in the skin of the wings where the antenna array is to be situated. The representation of the FEM is shown in Figure 1.3.

Figure 1.3 Simplified finite element model of antenna

A baseline configuration of the array was generated to correspond to the antenna orientation assuming the wing was not deformed. The antenna modelling software then generated the beam pattern. Phasing of the array elements was performed to generate the desired baseline beam orientation. Once this baseline was established, specific load configurations were applied to the lifting surfaces. Wing deformations were then be generated on a fully stressed design [2] by an integrated software environment utilizing the Adaptive Modeling Language (AML), MSC.NASTRAN and PanAir [10, 16, 22]. These deformations were used to determine the new location and slope of each element of the array. Figure 1.4 shows the typical deformed shape of the array compared to the undeformed shape. A new beam pattern was then generated. This process was repeated for the various load configurations. The results were compared to the baseline results to determine the beam pointing errors produced by the wing deformations.

Based on the location of the antenna arrays along the span of the wing sections, the placement and effectiveness of the control surfaces varies. The effectiveness was checked with just one control surface outboard of the wing joint. The process was not

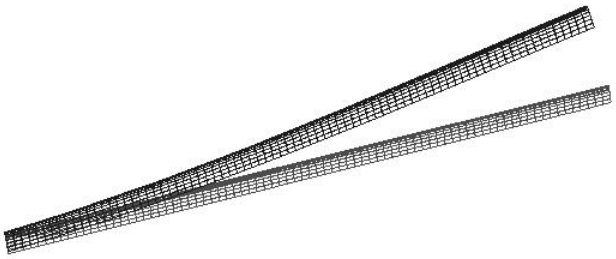

Figure 1.4 Deformed (upper) and undeformed (lower) configurations of the antenna array

optimized to determine the best configuration of the antennas and control surfaces. The antenna requirements drive the size of the array. The arrays must be placed inboard of the joint on both the front and aft wings. It was desired to have maximum control surface effectiveness while maintaining a 360^o beam coverage area around the perimeter of the aircraft.

1.5 Assumptions/Limitations

There were many aspects of this research that could have been explored in great depth, but this study was meant to set the foundation and basic theory of the interactions between the antennas and aircraft structure. Therefore, several assumptions were made in order to control the scope of this effort. These assumptions are broken down into three basic categories based on the outline of research objectives stated earlier: structural, antenna, and control surface effectiveness.

1.5.1 Structural. A simplified finite element model of the S-CLAS incorporating only the main load bearing layers of each element in the array was used.

By making this simplification, the number of layers of material in each element decreased from approximately 20 in the actual antenna down to only five in the FEM. This lay-up is shown in Figure 1.3 in the previous section.

The top layer of the FEM was assumed to be made of Astroquartz II RS12-B, which acts as an electromagnetically transparent layer to allow most of the antenna's energy to pass through unaffected. The second and fourth layers down from the top are made of honeycomb core material. These layers act essentially as spacers between the various elements of the antenna, but they also carry some shear load. The third and fifth layers are the main load-bearing parts of the antenna. They are two composite graphite epoxy (IM7/977-3) layers that act as a backplane (third layer) and a groundplane (bottom layer) in the antenna structure. Virtually the entire load is carried in these two layers. These properties for these materials are tabulated in Chapter 3.

1.5.2 Antenna. There were several assumptions made with respect to the antenna model. First, the actual conformal antenna element was much too complicated of a structure to accurately model in detail and incorporate into this study, given the time constraints and research objectives. Therefore horizontal dipoles were used instead of the actual elements. This allowed the theory to be more easily developed and verified. These dipoles gave the same polarization expected from the S-CLAS [15]. The baseline configuration of the antenna was assumed to be a linear translation out the span of one chordwise array of dipoles. The dipoles along one chord were positioned according to the geometric center of the actual square elements based on the assumed airfoil, LRN-1015 (see Appendix A). Their orientation was achieved assuming a simple translation in the chordwise direction due to wing twist and a central difference method in the spanwise direction to account for the rotation of the elements due to the wing deflection. Each chordwise array was assumed to be rotated as a single unit equal to the amount of rotation in the center

element of that particular chordwise array. It was also assumed that each individual dipole remained linear and was not allowed to bend.

When developing the equation of the magnitude of the electromagnetic field (E-field), far field assumptions were used. This means that the vectors pointing from the center of each element to the far field observation point were assumed to be parallel. Also, it was assumed that the magnitude and phase of the E-field radiated from each element could be summed in the far field. Therefore no mutual coupling between elements was accounted for in this approximation.

Another limitation was that this study did not take into account that the surrounding wing structure would have an effect on the antenna performance. For the purposes of this study, it was sufficient to place the elements in the correct geometrical configuration according to the position and geometry of the wing, but assume that they were operating in free-space with no degradation caused by the surrounding structure.

The current distribution along each dipole was assumed to be a cosine taper with zero current at both ends and a maximum value of one at the center. This current is more accurate than a constant current because the current on a real element must go to zero at the ends. The continuous curvature is also more practical than a triangularly shaped current. A closed form solution was then used for the Fourier Transform of this current. An explanation of the Fourier Transform is outlined in Appendix B.

1.5.3 Control Surface Effectiveness. The control surface effectiveness was derived by using a program called MSC.FlightLoads [11] and NASTRAN. FlightLoads was used to create an aerodynamic model with control surfaces and spline this together with the structural model. The control surface was assumed to be the rear half of the outboard portion of the joined wing. The aero/structure model was then processed using NASTRAN to derive the values necessary for calculating

the control surface effectiveness. FlightLoads utilizes a method compatible with the Doublet-Lattice method for subsonic flows and ZONA51 for supersonic flows. These methods represent the lifting surfaces as flat panels that are typically aligned with the flow. For further information on these calculations, the reader is referred to Reference [11].

1.6 Implications

This research allows for a quick approximation of the E-field radiated from an antenna ensemble of dipole elements that conform geometrically to a section of the wing surface given the coordinates of the center points of the elements. Plots are generated for the E-field magnitude for a baseline, undeformed wing and a deformed wing, and the percent change in the maximum amplitude is calculated. This gives the user an indication of the effect that wing deformation has on the pointing accuracy of the given antenna ensemble.

II. Literature Review

2.1 The Beginnings of the Joined-Wing Aircraft

Wolkovitch first developed the joined-wing aircraft in 1976 [23]. The basic idea of this design was that the aft wing was swept forward to connect with the trailing edge of the front wing. This configuration creates a diamond shape when viewing the aircraft from a front or top-down perspective. Wolkovitch also presented similar designs in 1982 [24], and in 1986 [25] he compared the performance of a joined wing to a conventional wing on a transport aircraft . He claimed that a joined wing had several advantages over conventional wings, namely low induced drag, high trimmed maximum coefficient of lift, and good stability and control.

Wolkovitch also found three other artifacts that are relevant to this study. First, he noted that the out-of-plane component of lift acting on the wing structure bends the wing about an axis that is tilted forward (see Figure 2.1). This phenomenon puts a downward pitching moment on the front wing, inducing a twist that is not present with conventional aircraft. This twisting motion is an important consideration for antenna arrays that conform to the surface of the wing because it adds another element of wing deformation besides the typical bending motion.

Secondly, Wolkovitch found from wind tunnel tests that several configurations of control surfaces were effective for pitch attitude control. He found, though, that using rear wing elevators does not create much additional lift on the front wing. This is an important consideration for the sensorcraft concept because wing "real estate" is limited due to the large size and number of sensors. He also noted that ailerons were more effective on the rear wing, especially if the front wing had a considerable dihedral angle.

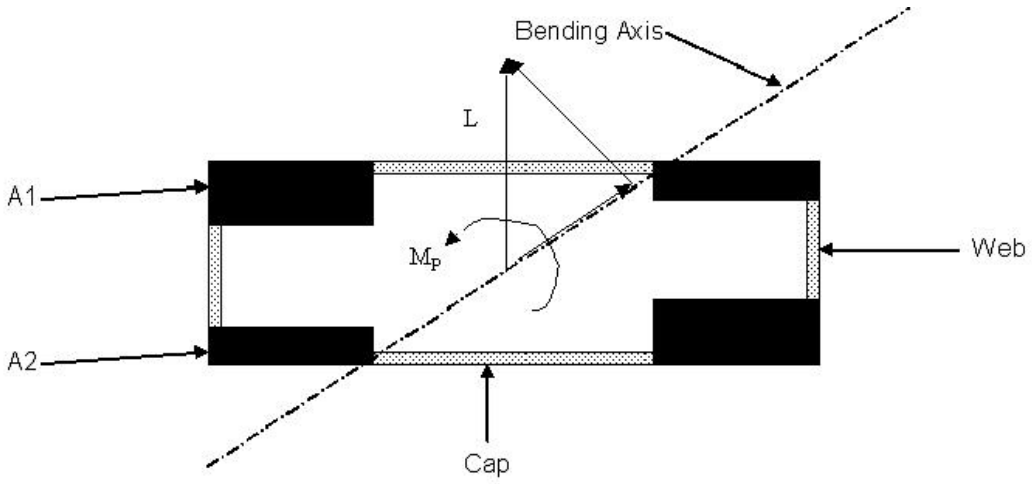

Figure 2.1 Modified wing-box structure to compensate for tilted bending axis of a joined wing showing components of lift and induced pitching moment.

2.2 Developing the Concept

Smith, Cliff, and Kroo, in conjunction with NASA Ames Research Center, designed a flight demonstrator aircraft with joined wings. Their objectives were to demonstrate good handling characteristics and validate the existing joined wing design methods. Their JW-1 design, a modified NASA AD-1 aircraft, was based on the idea that the joined-wing aircraft would be most beneficial as a medium-range transport due the potential weight savings offered by this type of configuration. Due to the requirement for good handling qualities, an emphasis was placed on improving the stall characteristics of the aircraft. To achieve this goal, Smith, Cliff, and Kroo decided to compromise cruise performance and add twist to the inboard section of the front wing. A small amount of additional twist was then needed in the aft wing in order to maintain an adequate amount of lift. By adding the twist in the wing to ensure correct stall characteristics, an 11% penalty was paid in the amount of induced drag during cruise [19]. Vortilons were also added to the configuration to counter an upward pitch that occurred at stall conditions. The vortilons remained on the aircraft for the remainder of the wind tunnel tests, including those for control surface effectiveness.

Various control surface configurations were investigated in this study. Control surfaces were segmented along the trailing edge of both the front and aft wings to allow each segment to act either independently or in concert. For example, by linking the two inboard segments (one on the front wing and one on the aft wing) and moving them equally in opposite directions, they found that pitch control could be achieved.

> A one-sixth scale wind tunnel model of the JW-1 design was built and tested in the NASA Ames 12-ft wind tunnel. Wind-tunnel-test data were used to assess performance, stability, and control, and to confirm that the relatively simple design tools used for the JW-1 are suitable for designing joined wings. [19]

A study was also performed [6] using the JW-1 in 1990, by Lin, Jhou, and Stearman, to determine the amount of influence that the type of joint has on the strength and stiffness of a joined wing. Eight different joint configurations were investigated in this study including a ball joint, pin joints, universal joint, link joints, and a rigid joint. They were interested in the influence of the joint on the distribution of stress and aeroelastic stability. All but the link joints and the telescoping joint reduced the bending moment in the front wing. "Only the rigid joint satisfies all of the other criteria of the minimum strain energy, most uniform strain energy density, and minimum level of joint reaction loads to accomplish the roll type bending moment reduction." [6] This study was somewhat limited due to the fact that linear modeling was employed and only under cruise flight conditions, but the study did ascertain that the fixed joint configuration is most likely the best overall choice for a joined-wing aircraft.

In another journal article [3], Gallman and Kroo, evaluated the weight optimization method and the fully stressed design method to compare the direct operating cost of conventional wing with joined-wing design. They determined that using a fully stressed design (FSD) based on non-linear analysis produces adequate results with much less computational time than a weight optimization method. They also

observed that adding a buckling criterion to the design caused the joined-wing to have a higher direct operating cost than the conventional aircraft. A FSD was used for the work [2] preceding this research, and FSD with non-linear analysis will be used throughout the remainder of this project. [18]

Livne surveyed these and over seventy other studies up through the year 2000 [7] in a study of the insights and limitations learned from aeroelastic and aeroservoelastic analysis and design of joined-wing configurations. In Livne's words, "there is still a basic lack of understanding of the structural and aeroelastic behavior and associated design issues and failure modes of such configurations." [7] He points out the need for research in the areas covered in the current work:

> Additionally, possible interactions on surveillance JW (joined-wing) aircraft between antennas built into the composite lifting surfaces and the structure itself should be studied. Such interactions involve both the effects on stiffness, damping and inertia of the integrated, multipurpose structure, and well as effects of antenna power consumption and heating. Strict stiffness requirements, imposed to meet precise antenna shapes and required electromagnetic performance can also add to the complexity of the MDO (multi-disciplinary optimization) problem. [7]

Livne also pointed out that the maneuver load factor and type of joint seem to be the most important factors of aeroelastic behavior, although the structural design of the lifting surfaces was also important.

M. Blair and R. Canfield used a FSD model of a joined wing in their work [2], which laid the foundation for the current study. Their efforts focused on creating a design process that generates reliable weight estimations of joined-wing aircraft. They wanted a design that simultaneously satisfies the range requirements, equilibrium in lift and pitching moment, and stress in static aeroelastic equilibrium. The structural and aerodynamic interface and non-linear trim were automated using the Adaptive Modeling Language (AML) to link ASTROS, NASTRAN and PanAir [22, 12, 8, 16] into a common design environment called the Air Vehicles Technology Integration Environment (AVTIE) [2]. A designer drives the analysis

with an AML interface. PanAir is used for the aerodynamic analysis. It calculates the aerodynamic load on the wing using a panel method. MSC.NASTRAN is used to investigate buckling in the wing and analyze the geometric nonlinearity of the model. The authors concluded that geometric nonlinearity is an important design consideration for a joined-wing aircraft and should be included in future models. An effort is currently underway to incorporate this nonlinearity into the design procedure. [18]

2.3 Integrating Antennas into the Joined-Wing Structure

Very little work has been documented with respect to integrating the antennas into the structure of a joined-wing aircraft. One relevant study investigated the use of a technology called Active Aeroelastic Wing in a joined-wing design to minimize the deformations of embedded antennas. [17] In this study, Reich, Raveh, and Zink concurrently used six control surfaces, as shown in Figure 2.2, to minimize wing deformation and trim the aircraft for 1-g level flight. While this is a novel approach to minimize the deformation of structurally integrated antennas, it is important to note that the antennas were strictly modeled as non-structural masses placed in the front and aft wings. The antennas were not load-bearing members of the structure, and therefore, the stiffness properties of the antennas were not incorporated into the design.

The results of this study show that the Active Aeroelastic Wing technology is a feasible concept for minimizing the wing deflection and thereby minimizing the antenna deformation. This will help to keep the degradation of the antenna performance to a minimum. Their research also points out that the most outboard and inboard, trailing edge control surfaces on the front wing appear to be the most effective for trimming the aircraft and "all three leading edge surfaces seem to be impractical trim devices."

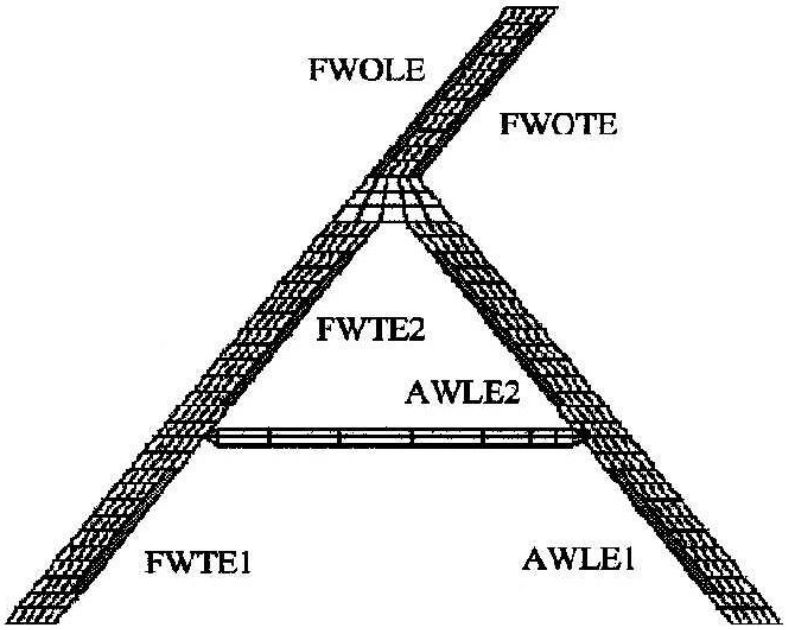

Figure 2.2 Description of control surfaces utilized for Active Aeroelastic Wing [17]

2.4 Conformal Antenna Theory

Virtually every text written on conformal arrays follows the same theoretical progression. Linear arrays are first established and characterized. Then groups of linear arrays are formed to make a planar array, and finally, a linear or planar array is wrapped around the surface of a cylinder to make a conformal array. W. H. Kummer follows this same logic in his paper [5] on basic array theory. He defines the array variations for his paper as follows:

> Linear arrays consist of equally spaced elemental radiators laid out in a straight line, while two-dimensional planar arrays consist of radiators oriented on a geometric grid in a plane. Rectangular arrays may be thought as a set of linear arrays placed next to each other, equally spaced, forming the two-dimensional array. A linear array may also be wrapped around a curved surface, usually a circle or a cylinder. Two-dimensional arrays can be formed by replicating these linear arrays along generatrices of cylinders and cones, or wrapping them on spheres. [5]

Kummer makes common simplifying assumptions in his analysis including a large distance from the source to the far-field region, thereby allowing a parallel ray approximation of the vectors pointing from each element to the far-field observation point. He also assumes that the elements are discrete with no coupling between elements, and they are arrayed in a repetitive grid with a constant distance between elements. Thus, he defines the electric field of the nth element in any array as:

$$\bar{E}_n(x,y,z) = (e^{-jkr}/r)\bar{A}_{e_n}(x',y',z')I_n \exp(jkr'_n \cos\xi_n). \tag{2.1}$$

The r term is the distance from the source to the observation point in the far-field region, and k is the wave propagation constant, which is $2\pi/\lambda$ in free-space with λ being the wavelength. $\bar{A}_e$ is a term that describes the electric field of one element by its polarization and orientation, I_n is the current applied to the nth element, and the phase excitation is described by the remaining exponential term. This equation is summed over all of the array elements, and the final equation describing any linear array consisting of n elements is given as:

$$\bar{E}(x,y,z) = (e^{-jkr}/r)\sum \bar{A}_{e_n} I_n \exp(jkr'_n \cos\xi_n). \tag{2.2}$$

The portion of this expression remaining in the summation is referred to as the array factor, A_a. It is based on the geometry of the array and not the elements themselves. Therefore different elements arrayed in the same way can be described using the same array factor.

Kummer then gives a discussion of linear array pattern analysis and synthesis by examining a four-element array aligned along the z-axis. One point of interest in this section is how the beam of the array is scanned by adding a phase progression, α , to the element current making $I_n = I_{0n}e^{-j\alpha(n-1)}$. "At the peak of the main beam, $\theta = \theta_0$, and the exponent equals zero, thus $\alpha = kd\cos\theta_0$," [5] where θ is the elevation angle of the main beam. The array factor then becomes

$$A_a = \sum_{n=1}^{N} I_{0n} \exp\left(j\left(n-1\right)\left[kd\left(\cos\theta - \cos\theta_0\right)\right]\right). \tag{2.3}$$

In this equation the value d is the uniform spacing between elements.

Linear arrays are then expanded into two-dimensional arrays by aligning linear arrays next to one another. A second summation of m elements is then required in the array factor for a planar array. The same logic for beam scanning as described previously is again applied to the planar array to allow scanning in this second dimension. Kummer pointed out that there is an angular limit to the amount that a planar array can effectively be scanned without significant losses. This limit is typically within 70^o of broadside (the vector normal to the plane). [5]

Conformal arrays are formed by wrapping linear or planar arrays around the surface of shapes such as cylinders, cones, and spheres. One of the main difficulties in analyzing conformal arrays is that the beam patterns of the elements can point in various directions. This means that the term describing the element pattern can no longer be factored out of the summations. An array of elements located on an arc of a circle, as shown in Figure 2.3, is examined. This array is projected onto a line that is perpendicular to the pointing direction of the main beam. This equivalent array is symmetric about the geometric center of the elements, but the spacing between each element is no longer constant.

Kummer's analysis of this configuration shows the development of large grating lobes at large scan angles. He concluded that linear/planar array techniques are not adequate for synthesizing conformal arrays.

Balanis develops his textbook [1] theory on arrays similar to that of Kummer. Balanis further elaborates on the phasing required for an end-fire configuration, where virtually all of the radiation is directed along the axis of the array. He chose to use β instead of α to represent the interelement phase progression, but otherwise the equations are the same. The total phase of a linear array, $\psi = kd\cos(\theta) + \beta$,

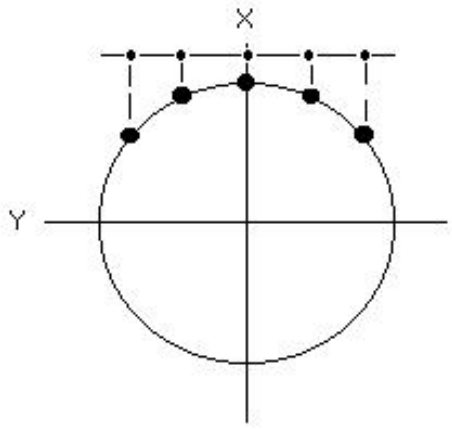

Figure 2.3 Array conforming to a circular arc projected onto a line forming an equivalent linear array with unequal spacing

where β is obtained by setting $\psi = 0$ with θ then becoming θ_0. It is important to note that this development allows β to be either positive or negative, depending on the desired angular location of the maximum amplitude, so it is important to use the correct value of θ_0 when steering the beam. Therefore, for an end-fire configuration, θ_0 is set equal to either 0^o or 180^o. One can also see that by progressively changing β, the direction of the maximum can be scanned between 0^o and 180^o.

Another parameter that Balanis explains has a large effect on the radiation pattern is the spacing between elements, *d*.

> If the element separation is $d = \lambda/2$, end-fire radiation exists in both directions ($\theta = 0^o$ and $\theta = 180^o$). If the element spacing is a multiple of a wavelength ($d = n\lambda$, n = 1, 2, 3, ...), then in addition to having end-fire radiation in both directions, there also exist maxima in the broadside directions. Thus for $d = n\lambda$, where n = 1, 2, 3, ..., there exist four maxima; two in the broadside directions and two along the axis of the array. To have only one end-fire maximum and to avoid any grating lobes, the maximum spacing between the elements should be less than $d_{max} < \lambda/2$. [1]

This methodology is easily extended for a rectangular array. In the XY-plane, the phase is separated into two components, ψ_x and ψ_y, where each takes into account the spacing and progressive phasing in their respective directions, given by

$$\psi_x = kd_x \sin\theta \cos\phi + \beta_x \tag{2.4a}$$

$$\psi_y = kd_y \sin\theta \sin\phi + \beta_y. \tag{2.4b}$$

Then for an m x n array with a uniform current, I_0, the array factor (AF) is comprised of two distinct summations as:

$$AF = I_0 \sum_{m=1}^{M} e^{j(m-1)(kd_x \sin\theta \cos\phi + \beta_x)} \sum_{n=1}^{N} e^{j(n-1)(kd_y \sin\theta \sin\phi + \beta_y)}. \tag{2.5}$$

Rewriting this equation in terms of sine functions and normalizing by the constant current magnitude the equation is then given as

$$AF_n(\theta, \phi) = \left\{ \frac{1}{M} \frac{\sin\left(\frac{M}{2}\psi_x\right)}{\sin\left(\frac{\psi_x}{2}\right)} \right\} \left\{ \frac{1}{N} \frac{\sin\left(\frac{N}{2}\psi_y\right)}{\sin\left(\frac{\psi_y}{2}\right)} \right\}. \tag{2.6}$$

Even though this equation was developed for isotropic point sources, it is useful because the total radiation field of an array of any type of elements can be found by multiplying the array factor of the isotropic source times the radiation pattern of the actual source. This pattern multiplication can be very useful for geometrically simple arrays, but every element in the array must be identical.

In the *Antenna Engineering Handbook* [9], R. J. Mailloux makes one other observation about conformal arrays that could be useful for certain applications of structurally embedded antennas. He points out that if the length of the array is small relative to the radius of curvature of the surface to which the array is conforming, then the array may be considered flat in order to simplify the problem. This means that the array may be treated as if it was planar, and the methods described above

can be utilized. He does not further quantify what ratio of length to radius is appropriate for this to be a reasonable approximation. The type of airfoil used in the aircraft design would determine the practicality of this assumption.

III. Methodology and Modeling

3.1 Antenna Structural Modeling

A simple structural model of the sensors was created, as shown in Figure 1.3, to incorporate the different layers of materials that make up the antenna's structure. The model has five layers that represent the main load bearing portions of the antenna. These finite element models were incorporated into the wing structure where the arrays are to be located, replacing the aluminum that was used for initial optimization efforts [18]. This allows a more accurate model of the wing structure to be generated. This also affects the overall stiffness of the structure, which in turn affects the amount of deflection in the wing. The simplified model consists of an electromagnetically transparent material called Astroquartz, honeycomb core material, and graphite epoxy. The top, outermost layer of the element is Astoquartz. This material covers the radiating parts of the antenna, protecting them from the atmosphere, while also allowing most of the antenna's energy to pass through with minimal resistance. There are two layers of graphite epoxy that act as the main load-bearing components of the antenna element. Both the Astroquartz and graphite epoxy layers were constructed of 0^o, $\pm 45^o$, and 90^o plies. Finally, two layers of honeycomb core material act as spacers between the other materials. It is in these two layers that the launchers, combiners, and other antenna components are located. Since these elements do not carry any of the loads, they can be ignored in the structural analysis. The thickness of each layer was established by Northrop Grumman [15] based on the required separation between various antenna components and optimization of the structure's weight and rigidity. The strength properties of each layer are outlined in Table 3.1.

Some additional values were also used for the honeycomb core layers [4]. Two shear moduli were given as 15.0 ksi and 8.0 ksi, corresponding to the L and W directions, respectively, as shown in Figure 3.1. Also, the density of the chosen

Table 3.1 Mechanical properties of Astroquartz, graphite epoxy, and honeycomb core [15, 4]

Material	$E_x\,[Msi]$	$E_y\,[Msi]$	ν_{xy}	$G_{xy}\,[Msi]$	$t_{ply}\,[in]$
Astroquartz	6.80	1.34	0.36	0.72	0.0055
Graphite Epoxy	22.13	2.15	0.3	0.6	0.0056
Honeycomb Core	0.07	0.07	—	0.0004	0.9/0.5

material was 4.5 lb/in^3, and the compressive strength was 560 ksi, which was assumed to be the same in both the x and y directions.

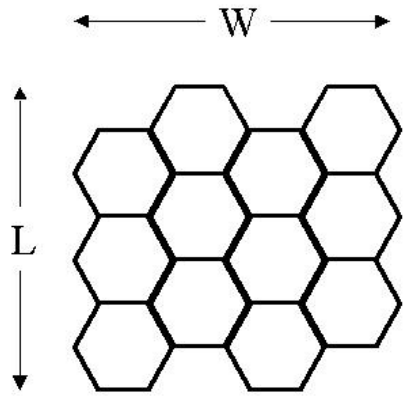

Figure 3.1 L and W directions of honeycomb core material

To test the validity of this model, buckling analysis was performed using NASTRAN on a rectangular mesh of these elements, which represented a typical wing skin panel. The panel was 33 inches in the span direction and 44 inches in the chord direction. The initial mesh contained 22 elements in each direction. A compressive load of 12,000 lbs./in was applied to the longer sides of the panel. This represented a spanwise load carried along the wing. The panel was clamped along the two longer, chordwise edges and simply supported along the other two spanwise edges. The first buckling mode eigenvalue and shape were obtained, and the mesh was then refined to test for convergence. The mode shapes were plotted using I-DEAS [20]. These results were compared to those generated by Northrop Grumman [15], and the results are shown in Chapter 4, Section 1.

3.2 Antenna Electromagnetic Model

The conformal load bearing antenna element is a complicated structure that would have been extremely difficult to model as a single entity. Therefore, it was decided that simple dipole (wire) antenna elements would be used to electromagnetically approximate the actual elements. Dipole antennas are one of the simplest antenna structures, and are widely used in the development of linear and planar array theory. All of the dipoles were assumed to be identical, perfect conductors with an infinitesimally small diameter.

The CLAS elements were designed to produce a horizontally polarized electric field. To represent this polarization, the dipoles were oriented parallel to the wing surface with 5 elements arrayed in the chordwise direction of the wing, conforming to the shape of the airfoil, and 40 elements in the spanwise direction. The $\hat{\phi}$ component of the electromagnetic field (see Equation 3.21) then describes the horizontally polarized portion of the total field.

A baseline configuration of the array was generated to correspond to the antenna orientation when the wing is not deformed. In this case the wing is assumed to be straight and at a fixed dihedral angle. The antenna array is positioned inboard of the wing joint and as close to the joint as possible considering the current 30^o wing sweep. This placement is shown in Figure 3.2.

The mesh used to generate the coordinate data file was created by intersecting the wing surface with $2N + 1$ planes in the spanwise direction, and $2M + 1$ planes in the chordwise direction, where N and M describe the number of elements in the spanwise and chordwise directions, respectively. The factor of two was used so that the coordinates of the center point of each element were obtained, as well as the coordinates for the point that bisected each side. Therefore, nine nodes described the location and orientation of each element. A section of a generic planar antenna with square elements is shown in Figure 3.3 to illustrate the nine node configuration.

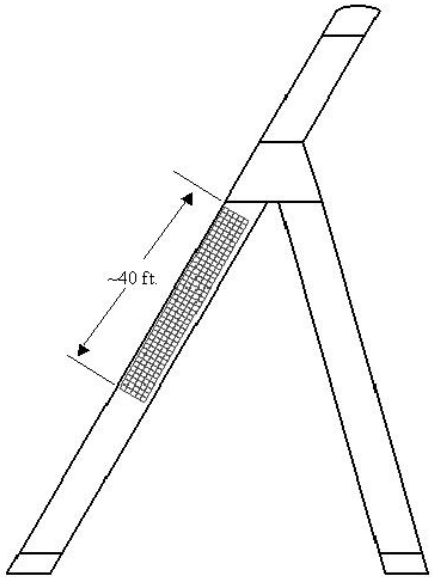

Figure 3.2 Antenna position on front section of joined wing

The two points in the middle of each element's chordwise side determined the length of the dipoles utilized in this analysis. For an antenna frequency of 430 MHz, this length was approximately half of a wavelength. The center points of the actual elements correspond to the center points of the dipoles. Initially, five dipoles were used to represent the five CLAS elements in the chordwise direction, but the final configuration of the dipoles utilized 10 dipoles to more closely model the effective spacing of the CLAS elements. The reasoning behind this change is further explained in the next chapter.

Two other versions of the array were used besides the 10x40 front wing array. First the array size was increased to 10x60 elements on the front wing. This version is shown in Figure 3.4. The second version placed a 10x60 element array in the aft wing section, which is shown in Figure 3.5.

End-fire phasing was applied to steer the main beam straight out from the leading edge and in the plane of the wing. Once the baseline pattern was established for

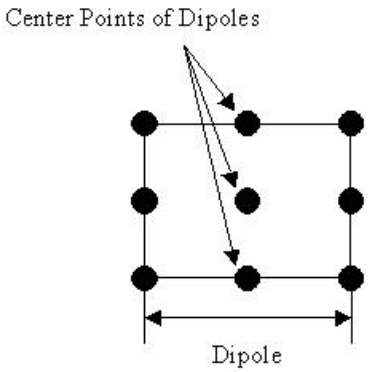

Figure 3.3 Nodes on square, S-CLAS element representing where coordinates are required for analytical development of the dipole array

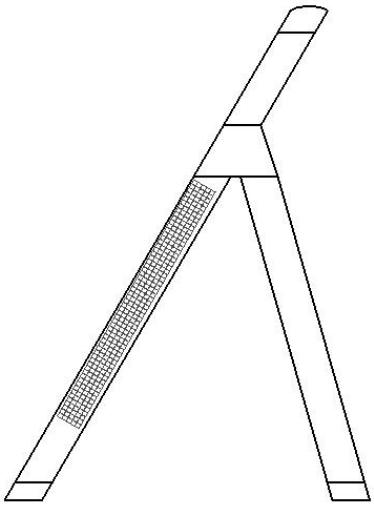

Figure 3.4 10x60 element array located on the front wing section

the undeformed case, specific load configurations were applied to the lifting surfaces. Wing deformations were then generated on a fully stressed design [18] by an integrated software environment called AVTIE [2], which utilizes the Adaptive Modeling Language (AML), MSC.NASTRAN and PanAir [22, 8, 16]. These deformations were used to determine the new location and slope of each element of the array. Figure 1.4 shows the typical deformed shape of the array compared to the undeformed shape. A new beam pattern was then generated. This process was repeated for various

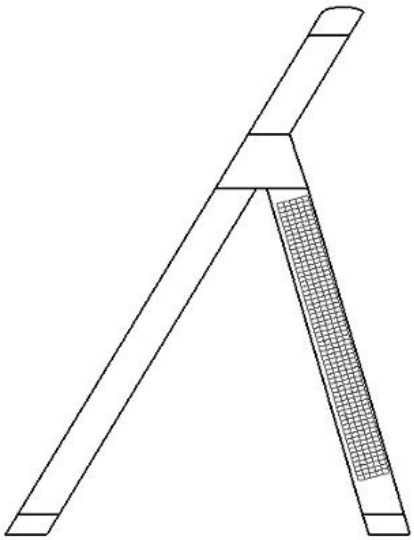

Figure 3.5 10x60 element array located on the aft wing section

load configurations. The results were compared to the undeformed wing results to determine the beam pointing errors produced by the wing deformations.

The radii of curvature of the top and bottom surfaces of the wing were also checked to see whether Mailloux's flat array approximation could be applied. The local radius of curvature of a point on the airfoil was determined based on its location relative to two adjacent points. These three points defined an arc of a circle and the radius of that circle was then calculated by symbolically solving a system of three simultaneous equations. The three equations were

$$(x_1 - x_0)^2 + (y_1 - y_0)^2 - r^2 = 0 \tag{3.1a}$$

$$(x_2 - x_0)^2 + (y_2 - y_0)^2 - r^2 = 0 \tag{3.1b}$$

$$(x_3 - x_0)^2 + (y_3 - y_0)^2 - r^2 = 0 \tag{3.1c}$$

where x_0 and y_0 were the coordinates of the center of the circle with radius, r, formed by the three points with coordinates, x_i and y_i, $i = 1, 2, 3$. The LRN-1015 airfoil is shown in Figure 3.6.

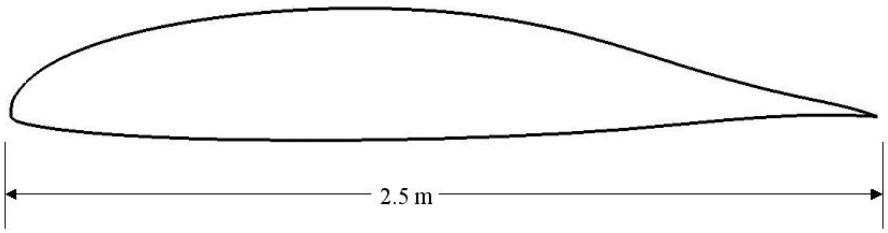

Figure 3.6 LRN-1015 airfoil

A frequency of 430 MHz corresponds to a wavelength of 27.5 inches. Therefore, the chordwise length of the array was approximately 2.5 wavelengths. A radius was assumed to be much larger than this array length if it was over 10 times the wavelength.

3.3 Array Theory

Developing the theory for this array began by defining the geometry and orientation of the array. The implementation was general enough to analyze any array. This allowed the same code to be utilized for the array under any load configuration. The coordinates were given in terms of a global wing reference frame, where the origin was located at the leading-edge of the root of the wing. The orientation of the x and y axes with respect to the wing are shown in Figure 3.7.

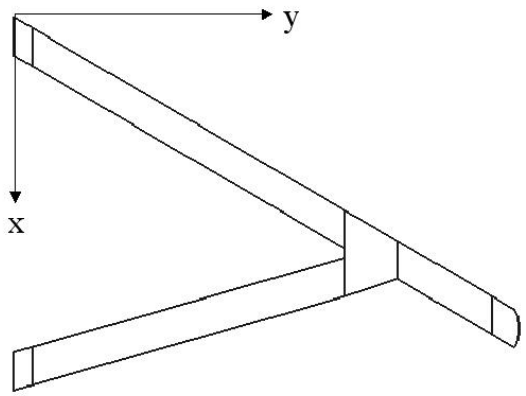

Figure 3.7 Global wing coordinate reference frame

The reference frame utilized in the array development was a clockwise rotation of the x and y axes in the global reference frame corresponding to the wing sweep. The origin was also translated to coincide with the center point of the dipole situated in the inboard, leading-edge corner of the array, which was defined to be the original element that was arrayed to form the entire sensor suite. This reference frame is shown in Figure 3.8. Two chordwise arrays of dipoles were drawn into this figure to illustrate that the origin of the array reference frame coincided with the center point of the inboard, leading-edge dipole, and the $\hat{y}$-axis lined up parallel to the same inboard, leading-edge dipole. Therefore, wherever that particular dipole was situated on the wing defined the location and orientation of the array coordinate system.

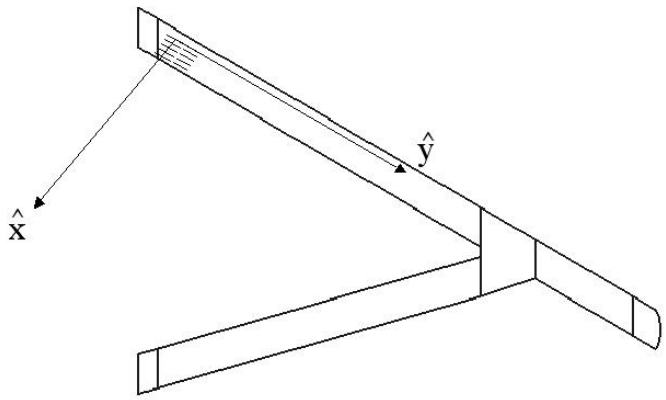

Figure 3.8 Antenna coordinate reference frame with two inboard chordwise arrays drawn in for reference

A vector, $\vec{r}_0$, was formed to point from the origin to any point on the dipole centered at the origin of the coordinate reference frame, given by

$$\vec{r}_0 = y\hat{y} \tag{3.2}$$

The value y corresponds to a position along the length of each dipole. For the undeformed wing case, all of the dipoles are assumed to be aligned parallel to the $\hat{y}$ direction.

Next, a vector was formed that points from the center of the original element to the center point of the kth element in one chordwise array,

$$\vec{r}_k = (x_k - x_0)\hat{x} + (y_k - y_0)\hat{y} + (z_k - z_0)\hat{z}. \tag{3.3}$$

Since the original dipole was assumed to be centered at the origin of the antenna reference system, this equation can be simplified to

$$\vec{r}_k = x_k\hat{x} + y_k\hat{y} + z_k\hat{z}. \tag{3.4}$$

Equations 3.2 and 3.4 were then summed to give a new vector that points from the origin to any point on the kth dipole,

$$\vec{r}'_k = \vec{r}_0 + \vec{r}_k. \tag{3.5}$$

A third vector was also defined. This was a unit vector that pointed in the direction of an observation point in the far-field of the antenna. This vector is defined as follows:

$$\hat{r}(\theta, \phi) = \hat{x}\sin\theta\cos\phi + \hat{y}\sin\theta\sin\phi + \hat{z}\cos\theta \tag{3.6}$$

where elevation, θ, and azimuth, ϕ, are defined according to Figure 3.9.

For evaluation purposes, the position of the observation point was varied to give three "great circle" cuts. In each cut one angle was held fixed while the other was varied from 0 to 2π. To get an elevation cut, ϕ was set equal to 180^o. For an azimuth cut, θ was set to 90^o. Finally, for the third cross-sectional cut, ϕ equaled

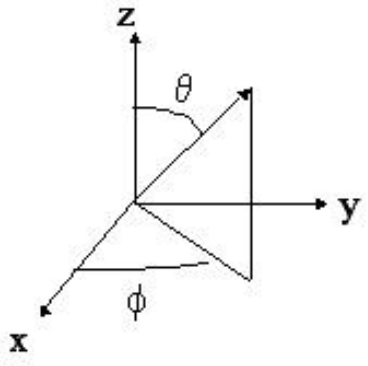

Figure 3.9 Array coordinate system

90^o and θ was varied. These three cuts are the most common for defining radiation patterns.

The phase of the array in free space was then described by the expression $e^{j\beta\vec{r}_k'\cdot\hat{r}}$, where β is again the wave propagation constant for lossless space, $\beta\hat{=}\omega\sqrt{\mu\epsilon}$. In this equation for β, μ and ϵ are the permeability and permittivity, respectively, of the material surrounding the antenna, and the angular frequency, ω, is defined as $\omega = 2\pi f$, where f is the operating frequency of the antenna. Substituting Equation 3.5 into the dot product, the phase then becomes $e^{j\beta(\vec{r}_0\cdot\hat{r}+\vec{r}_k\cdot\hat{r})}$.

A cosine current distribution was applied to each dipole. This distribution is defined by a maximum value of 1 at the center of the dipole, going to zero at each end. The cosine function was chosen because it had no discontinuities along the length of the dipole, and it matched the boundary conditions of the current going to zero at both ends of the dipole. The current was a complex vector quantity (represented by a bar under the symbol) defined below:

$$\underline{\bar{J}}_R(\theta,\phi,\omega) = \sum_k \hat{y} a_k e^{j\delta_k} \cos\left(\frac{\pi}{L} y_k\right) \tag{3.7}$$

where a_k was a weighting coefficient that could be used to scale the magnitude of the current on the kth element, and L is the length of the dipoles, which was $\frac{\lambda}{2}$.

The free space wavelength λ is defined as $\lambda \hat{=} \frac{2\pi}{\beta}$. The coefficient a_k was simply set to a value of one for all elements for the purpose of this study, but it was important to incorporate into the derivation for future work to optimize the radiation pattern. The interelement phasing, δ_k, was applied to each element to steer the main beam in the desired direction. The subscript R denotes that this equation was derived for a rectangular coordinate system, and it is a function of elevation, θ, azimuth, ϕ, and the angular frequency, ω, which is 2π times the radial frequency of the system.

This equation was then expressed in term of the frequency domain through the use of a Fourier Transform. The equation of the transform was as follows:

$$\underline{\bar{\mathcal{J}}}_R(\theta, \phi, \omega) = \int_{\vec{r}'_k} \underline{\bar{J}}_R e^{j\beta(\vec{r}_0 \cdot \hat{r} + \vec{r}_k \cdot \hat{r})} d\vec{r}'_k \tag{3.8}$$

An assumption was made here that loss is ignored in the integral. This assumption is valid because the loss has no effect on frequency, and it is transverse to the main direction of propagation and loss, which is in the direction of $\hat{r}$.

Taking the derivative of Equation 3.5 and assuming that the kth element is at a fixed point in space, then

$$d\vec{r}'_k = d\vec{r}_0. \tag{3.9}$$

Noting also that the derivative of $\vec{r}_0$ with respect to y_k is simply dy_k, a change of variables was performed on Equation 3.8, and the equation for $\underline{\bar{\mathcal{J}}}_R$ became

$$\underline{\bar{\mathcal{J}}}_R(\theta, \phi, \omega) = \int_{y_k} \underline{\bar{J}}_R e^{j\beta(\vec{r}_0 \cdot \hat{r} + \vec{r}_k \cdot \hat{r})} dy_k. \tag{3.10}$$

The constant terms were then removed from the integral, and the final form of this equation before the transform is performed is shown below:

$$\underline{\bar{\mathcal{J}}}_R(\theta,\phi,\omega) = \hat{y}\left[\sum_k a_k e^{j\delta_k} e^{j\beta\hat{r}\cdot\vec{r}_k}\right] \int_{y_k} \cos\left(\frac{2\pi}{\lambda} y_k\right) e^{j\beta\hat{r}\cdot\vec{r}_0} dy_k. \tag{3.11}$$

A detailed explanation of the Fourier Transform is given in Appendix B. A closed form approximation was used for this study to simplify the transform. Therefore, the integral portion of Equation 3.11 results in the following expression:

$$\int_{y_k} \cos\left(\frac{2\pi}{\lambda} y_k\right) e^{j\beta\hat{r}\cdot\vec{r}_0} dy_k = \frac{\frac{\pi}{L}\cos(u)}{1-\left(\frac{2u}{\pi}\right)^2}, \tag{3.12}$$

where L is the length of the dipole, and u for a $\hat{y}$-directed current is defined as

$$u = \frac{L}{2}\sin\theta\sin\phi. \tag{3.13}$$

Substituting Equations 3.12 and 3.13 back into Equation 3.11, the transformed current became

$$\underline{\bar{\mathcal{J}}}_R(\theta,\phi,\omega) = \hat{y}\left[\sum_k a_k e^{j\delta_k} e^{j\beta\hat{r}\cdot\vec{r}_k}\right]\left[\frac{\frac{\lambda}{\pi}\cos\left[\frac{L}{2}\sin(\theta)\sin(\phi)\right]}{1-\left(\frac{L}{\pi}\sin(\theta)\sin(\phi)\right)^2}\right] \tag{3.14}$$

where

$$\hat{r}\cdot\vec{r}_k = (x_k - x_0)\sin\theta\cos\phi + (y_k - y_0)\sin\theta\sin\phi + (z_k - z_0)\cos\theta \tag{3.15}$$

A vector potential, $\underline{\vec{A}}_R$, in rectangular coordinates was then created. This is common practice when solving Maxwell's Equations, because it allows a difficult integration to be broken up into a simpler integration and differentiation steps as shown in Figure 3.10. The vector potential in a lossless medium is defined as

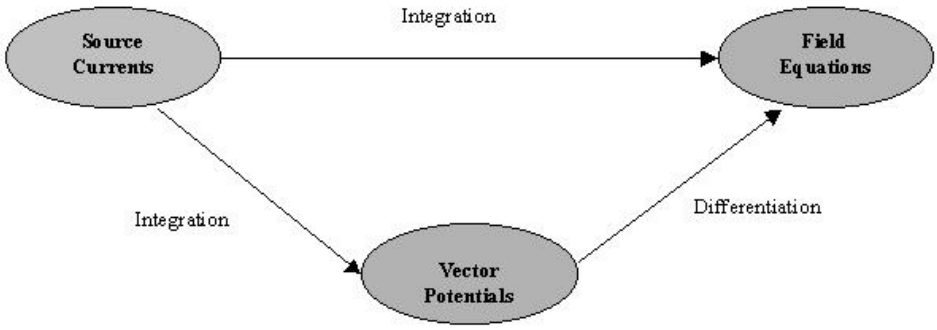

Figure 3.10 Pictorial representation of the use of vector potentials to find the electromagnetic fields

$$\underline{\vec{A}}_R = \mu_o \Psi(r,\omega)\underline{\bar{\mathcal{J}}}_R. \tag{3.16}$$

where μ_o is the permeability of free-space (4πx10^{-7}), and $\Psi(r,\omega)$ is the radial component of Green's Function in free-space defined as follows:

$$\Psi(r,\omega) = \frac{e^{-j\beta r}}{4\pi r} \tag{3.17}$$

where r is the distance from the source to the far-field observation point.

The vector potential was then transformed from rectangular to spherical coordinates by use of the transformation matrix, T_S^R.

$$\overline{\overline{T}}_S^R = \begin{bmatrix} \sin\theta\cos\phi & \sin\theta\sin\phi & \cos\theta \\ \cos\theta\cos\phi & \cos\theta\sin\phi & -\sin\theta \\ -\sin\phi & \cos\phi & 0 \end{bmatrix} \tag{3.18}$$

Since the current was assumed to be oriented entirely along the $\hat{y}$-axis, the $\hat{x}$ and $\hat{z}$ components of $\underline{\vec{A}}_R$ were set equal to zero, and $\underline{A}_y$ was multiplied times the transformation matrix. Also, the radial component of the vector potential in spherical form was discarded based on the far-field assumption that there is no variation in the radial direction. This resulted in the following equation:

$$\underline{\bar{A}}_S = \overline{\overline{T}}_S^R \cdot \underline{\bar{A}}_R. \tag{3.19}$$

The far-field region E-field in spherical coordinates minus the radial component was then defined as

$$\underline{\bar{E}}_S = -j\omega \left[\underline{\bar{A}}_S - \hat{r}\underline{A}_r\right]. \tag{3.20}$$

Expanding this, the equation for the E-field was as follows:

$$\underline{\bar{E}}_S = -j\omega\mu_o \frac{e^{-j\beta r}}{4\pi r}\left[\sum_k a_k e^{j\delta_k} e^{j\beta\hat{r}\cdot\vec{r}_k}\right]\left[\frac{\frac{\lambda}{\pi}\cos\left[\frac{L}{2}\sin\theta\sin\phi\right]}{1-\left(\frac{L}{\pi}\sin\theta\sin\phi\right)^2}\right]\left[\hat{\theta}\cos\theta\sin\phi + \hat{\phi}\cos\phi\right] \tag{3.21}$$

where, for horizontal dipoles, the $\hat{\theta}$ component corresponds to the vertically polarized portion of the equation, and the $\hat{\phi}$ component corresponds to horizontal polarization. Since this study was interested in emulating a horizontally polarized field, only $\underline{E}_\phi$ was used. Therefore the plots that were generated correspond to:

$$\left|\underline{\bar{E}}_\theta\right| = -j\omega\mu_o \frac{e^{-j\beta r}}{4\pi r}\left[\sum_k a_k e^{j\delta_k} e^{j\beta\hat{r}\cdot\vec{r}_k}\right]\left[\frac{\frac{\lambda}{\pi}\cos\left[\frac{L}{2}\sin\theta\sin\phi\right]}{1-\left(\frac{L}{\pi}\sin\theta\sin\phi\right)^2}\right]\cos\phi. \tag{3.22}$$

The MATLAB code used to plot the three Great Circle cuts of Equation 3.22 breaks the sum on k into two summations: one to sum the elements in the chordwise direction, forming a chordwise array, and then a second to sum up all of the chordwise arrays. This summing process was a simplification that originates from the far-field planar array theory.

Thus far, the equations were developed assuming that the wing was undeformed. Therefore it was assumed that each new dipole orientation and location

was strictly due to a translation of the element from the origin. For a deformed wing this assumption was no longer valid, and the amount of rotation experienced by each element had to be calculated and incorporated into the radiation pattern equations. To accomplish this, the same data file described in Section 3.2, page 3-3, was used in conjunction with a central difference formula to calculate the slope of each dipole. The central difference formulation utilizes the y and z coordinates of the data points. A forward difference method was used to characterize the slope of the elements along the inboard edge of the array, and a backward difference was used along the outboard edge. These equations are defined as follows:

$$slope(n,1) = \frac{z(n,2) - z(n,1)}{h} \tag{3.23}$$

$$slope(n,m) = \frac{z(n,m) - z(n,m-1)}{h} \tag{3.24}$$

where h was the difference in y of adjacent nodes, which equals $y(n,2) - y(n,1)$ in Equation 3.23 and $y(n,m) - y(n,m-1)$ in Equation 3.24. The indices n and m describe the number of data points in the chordwise and spanwise directions, respectively.

For the interior points of the array, the following equation was used:

$$\begin{aligned} slope(n,m+1) &= \frac{\left(-\frac{h(n,m+1)}{h(n,m)} z(n,m) + \frac{h(n,m)}{h(n,m+1)} z(n,m+2)\right)}{h(n,m) + h(n,m+1)} \\ &+ \left(\frac{1}{h(n,m)} - \frac{1}{h(n,m+1)}\right) z(n,m+1). \end{aligned} \tag{3.25}$$

This new orientation of each dipole was then incorporated into Equation 3.13. This equation, which described the orientation of the current on each dipole, then became

$$u(n,m) = \frac{L}{2}(\cos(slope(n,m)) \sin\theta \sin\phi + \sin(slope(n,m)) \cos\theta), \tag{3.26}$$

and was used as before in the equation describing the E-field, Equation 3.21.

With the dipoles situated parallel to the surface of the wing, any twist in the wing resulted in only a translation of the dipole. These translations were accounted for in the vector r_k, since it pointed to the center of the dipole in its new position. The data files used to generate the patterns for the deformed wing cases included the trim angle of attack and aft wing rigid twist that correspond to each load case. Therefore, the trimmed angle of attack was subtracted from the main beam pointing angle results so that only changes due to wing deflection are present for the array in the front wing. For the aft wing array, the twist required to trim for pitch remained in the results, because the twist is not constant out the span of the aft wing. For the 2.5g maneuver load the trim angle of attack was 0.26^o, and the aft wing twist was -4.23^o. For the gust load case, the angle of attack was 1.28^o and the aft wing twist was 1.08^o.

3.4 Computational EM Method

For comparison purposes, the model was also analyzed with a numerical electromagnetic code that solves for the radiation pattern of the array using a method of moments technique. The software package is called NEC-Win Plus+^{TM}, and it is a scaled down, more user-friendly version of the full NEC software [14]. It allows simple antenna models to be built fairly quickly, and it can numerically determine their electromagnetic response for a given current excitation. The properties for the antenna array were defined to have a frequency of 430 MHz, no ground plane, a characteristic impedance of 50 Ohms, each wire constructed of 11 segments, a current source at the center of the wire, current magnitude of 1.0, a wire diameter of 0.001 meters, a perfectly conducting wire, and 90^o phasing applied from one element to the next in the chordwise direction. The electric field integral equation was described in the previous section, but there a closed form solution was used to approximate the solution of the Fourier Transform due to the simplicity of the elements. NEC-

Win Plus+^{TM} numerically solves these equations to give a closer approximation of the exact solution. This process assumes nothing about the orientation of one element with respect to another. By using this software, it was possible to see how applicable basic array theory was for the given array. It was preferable to use the MATLAB code, because it was computationally less intensive and could be more easily incorporated into the aircraft design environment.

The method of moments is a general technique for approximating the solution of linear operator equations. It does this by creating a system of simultaneous linear equations that represent the linear operator equation. For example, the linear operator equation

$$Lf = g \tag{3.27}$$

consists of the linear operator, L, the unknown function, f, and some known function, g. In the context of electromagnetics, one typically knows the integral equation describing the electric or magnetic field. This corresponds to the linear operator, and g represents the known excitation of the system (i.e. source currents). The unknown function, f, is therefore the radiated energy due to the excitation. A series expansion is used to approximate the unknown function.

$$f = \sum_n a_n I_n \tag{3.28}$$

In this equation, a_n is a scalar coefficient applied to the basis function, I_n. The choice of basis functions determines the accuracy of the solution. Therefore, a great amount of consideration typically goes into selecting appropriate basis functions for a given system. The reader is referred to the NEC manual [13] for a complete derivation of the basis functions which satisfy the boundary conditions for wire elements.

An inner product of two functions is then defined as follows:

$$\langle \chi, \eta \rangle = \int_S \chi(\vec{r})\eta(\vec{r})dA \tag{3.29}$$

integrating over the entire surface of the system. The inner product is taken of Lf and a set of test functions, w_m. The NEC code chooses these test functions to be delta functions,

$$w_m(\vec{r}) = \delta(\vec{r} - \vec{r}_m) \tag{3.30}$$

where $\vec{r}$ points to the far-field observation location, and $\vec{r}_m$ points to a location on the surface of the antenna. These points on the surface of the antenna are the center points of each segment on every antenna. This point sampling method was the main reason why this approach took a considerable amount of time and computer capacity. For the antenna array studied, this corresponded to 400 elements with 11 segments each, or 4400 points at every angular step in a 360^o observation range.

The inner product of Equation 3.27 and the test functions is

$$\langle w_m, Lf \rangle = \langle w_m, g \rangle \,, \tag{3.31}$$

where $m = 1, 2, 3, \ldots, N$. Equation 3.28 is then substituted into this equation. The resulting inner product is then

$$\sum_{n=1}^{N} a_n \langle w_m, LI_n \rangle = \langle w_m, g \rangle \,. \tag{3.32}$$

This equation can be written in matrix form as

$$[Z]\,[A] = [G] \tag{3.33}$$

where the matricies are defined as follows:

$$[Z] = \begin{bmatrix} \langle w_1, LI_1 \rangle & \langle w_1, LI_2 \rangle & \cdots \\ \langle w_2, LI_1 \rangle & \langle w_2, LI_2 \rangle & \cdots \\ \vdots & \vdots & \ddots \end{bmatrix} \tag{3.34}$$

$$[A] = \begin{bmatrix} A_1 \\ A_2 \\ \vdots \end{bmatrix} \tag{3.35}$$

$$[G] = \begin{bmatrix} \langle w_1, g \rangle \\ \langle w_2, g \rangle \\ \vdots \end{bmatrix}, \tag{3.36}$$

and the solution is

$$[\mathrm{A}] = [\mathrm{Z}]^{-1}[G]. \tag{3.37}$$

In an electromagnetic context, Z is typically referred to as the impedance matrix, G is the excitation vector, and A is called the current vector. Based on this derivation, Equation 3.28 then becomes

$$f = \sum_{n=1}^{N} A_n I_n \tag{3.38}$$

for the chosen set of basis functions, I.

3.5 Control Surface Effectiveness

An aerodynamic model was created using MSC.FlightLoads [11]. The model was generated for a 2.5g pull-up maneuver at the end of the mission profile (i.e. landing), therefore sea level conditions were assumed. This model consisted of four main sections: the front wing inboard of the joint, the aft wing inboard of the joint, the joint, and the remainder of the wing outboard of the joint (wing tip). The aerodynamic model is shown in Figure 3.11. An aileron was placed in the wing tip

section of this model and used to trim for pitch so the effectiveness of this control surface could be determined. This control surface was sized to be 30% of the chord length and half of the span length of the wing tip section, and located along the trailing edge of the wing tip section as far outboard as possible.

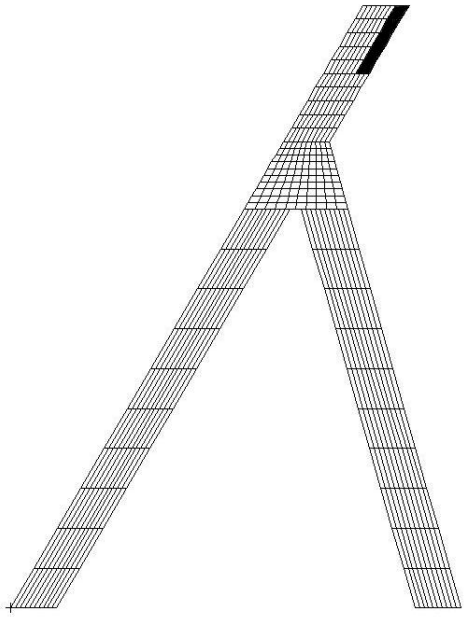

Figure 3.11 Aerodynamic panel model of joined wing with shaded panels showing location of aileron

Once the aerodynamic model was built, FlightLoads was used to spline it to the structural model. FlightLoads then generated a NASTRAN input file, and it was analyzed to find the static aeroelastic response of the model. From the NASTRAN output file, the coefficient of lift per unit change in control surface deflection (δ) of an elastic wing, $C_{L_\delta}(elastic)$, and the coefficient of lift per unit change in δ of a rigid wing, $C_{L_\delta}(rigid)$, were obtained. These two values are used to define the control surface lift effectiveness, η_L, as follows:

$$\eta_L = \frac{C_{L_\delta}(elastic)}{C_{L_\delta}(rigid)}. \tag{3.39}$$

The purpose of an aileron is not to trim the aircraft for pitch, so this effectiveness was expected to be quite low. If control surfaces are not effective for pitching the aircraft, though, other options must be utilized. This meant that either the aft wing had to twist to trim the aircraft for pitch, or a control surface had to be placed somewhere inboard of the joint, which would limit the maximum size of the antenna arrays. It was decided that aft wing twist would be used. Therefore, the effectiveness of the aileron was checked for its intended purpose, which was to roll the aircraft. NASTRAN was used to find the non-dimensional roll rate, $\frac{pb}{2V\delta}$, at which aileron reversal occurred, where p is the roll rate, b is the total span, V is the velocity, and δ is the aileron deflection. The dynamic pressure, $\bar{q}$ (and therefore the velocity) related to the reversal condition was also found. The results of this analysis are shown in Section 4.5.

IV. Results

4.1 FEM Results

The composite antenna elements were examined by creating a rectangular 33"x44" mesh, similar to a wing panel, consisting of these elements. This was done in an effort to duplicate results generated in a similar proprietary effort by Northrop Grumman [18], thereby validating this model. Northrop Grumman's three-dimensional FEM was more robust than the two-dimensional model developed for this study, but the model used gave a first buckling mode eigenvalue that was within acceptable limits of Northrop Grumman's results, considering the current fidelity of the entire joined-wing model.

The first buckling mode eigenvalue was 1.27 for the panel under a spanwise compressive load on the two longer edges with all of the edges simply supported. This mode shape is shown in Figure 4.1. Northrop Grumman's value for this mode was 0.99. It was believed by Northrop Gurmman that a more realistic representation of the constraints had the chordwise edges clamped and the spanwise edges simply supported. Therefore, the boundary conditions were changed to reflect these conditions. The eigenvalue remained the same, but the mode shape changed to two sine waves, as shown in Figure 4.2, instead of one and a half in the case where all of the edges were simply supported . Northrop Grumman's eigenvalue for this clamped/simply supported condition was 1.31, and the mode shape looked similar to Figure 4.3.

Figure 4.3 was achieved for the model developed in this effort by decreasing the overall element thickness. This result was not used because the thickness of each layer was assumed to be significant to the sensor performance. Decreasing the thickness would have altered the distance between the various parts of the antenna, essentially producing a different antenna element. Also, the intent was to validate

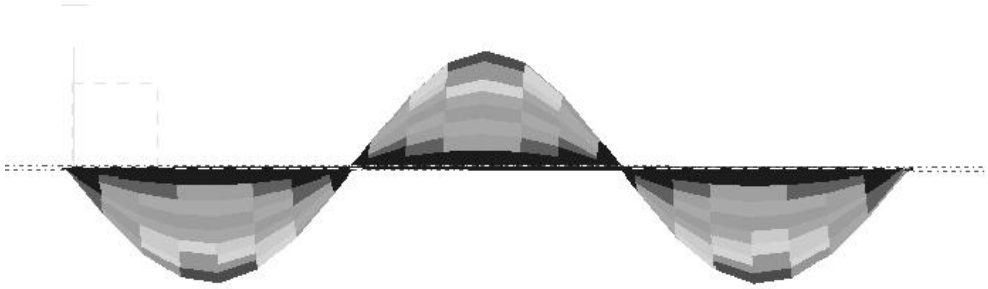

Figure 4.1 First buckling mode shape for all edges simply supported

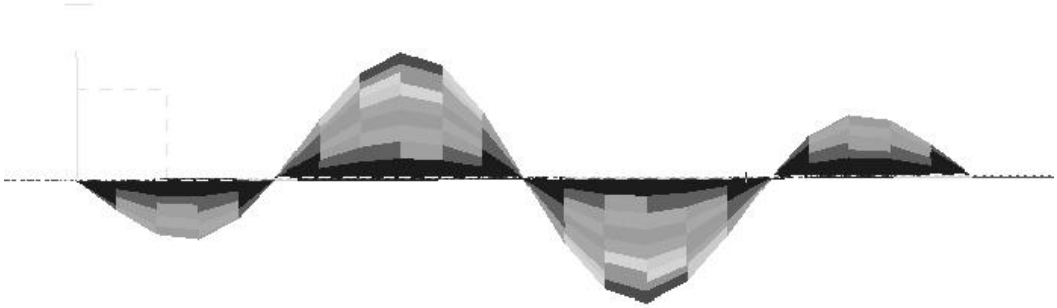

Figure 4.2 First buckling mode shape with chordwise edges clamped and spanwise edges simply supported

the stiffness of the current model, and not to reproduce the exact results achieved by Northrop Grumman.

4.2 Airfoil Curvature

The radius of curvature calculations found that 40% of the bottom surface of the wing had a radius of curvature greater than 10 times the wavelength, λ. Approximately 71% of the top surface of the wing had a radius of curvature that did not meet the length criteria, which suggested that an array could be considered flat only if the local radius of curvature was greater than 10λ. A series of plots is shown in Figure 4.4. The top plot shows the shape of the airfoil as a reference, the

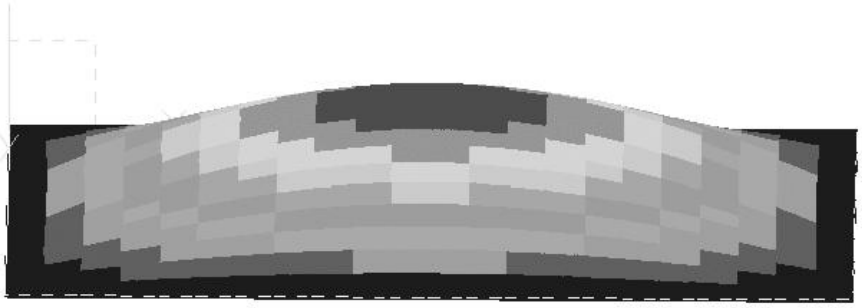

Figure 4.3 Half sine wave mode shape

middle plot is the absolute value of the radius of curvature of the top surface, and the bottom plot is the absolute value of the radius of curvature of the bottom surface. The main array structure was assumed to fit between the leading and trailing edge spars. Looking at the plot of the airfoil, the leading edge spar was at an x-coordinate of 11.96 inches, or 12.2% of the chord, and the trailing edge spar was at 73 inches, or 74.5% chord. With the added wing deformation, neither the top nor bottom surface remains planar regardless of the chordwise curvature. For these reasons, the flat array approximation was not considered for this study.

4.3 Pattern Computation with NEC-Win Plus+^{TM}

NEC-Win Plus+^{TM} was also used to obtain radiation patterns for the conformal array of dipoles on the undeformed wing and in the case where a gust load was applied to the wing. NEC-Win Plus+^{TM} will only plot the gain pattern of the array in dB, but the basic shape of the radiated pattern should be similar whether the plot is gain or simply the field magnitude plotted in $\frac{V}{m}$. The radiation pattern of a 10x40 element array located close to the fuselage was calculated for the undeformed wing and the gust load case. The results from the basic array analysis are shown in Figures 4.5, 4.6, 4.7, and 4.8.

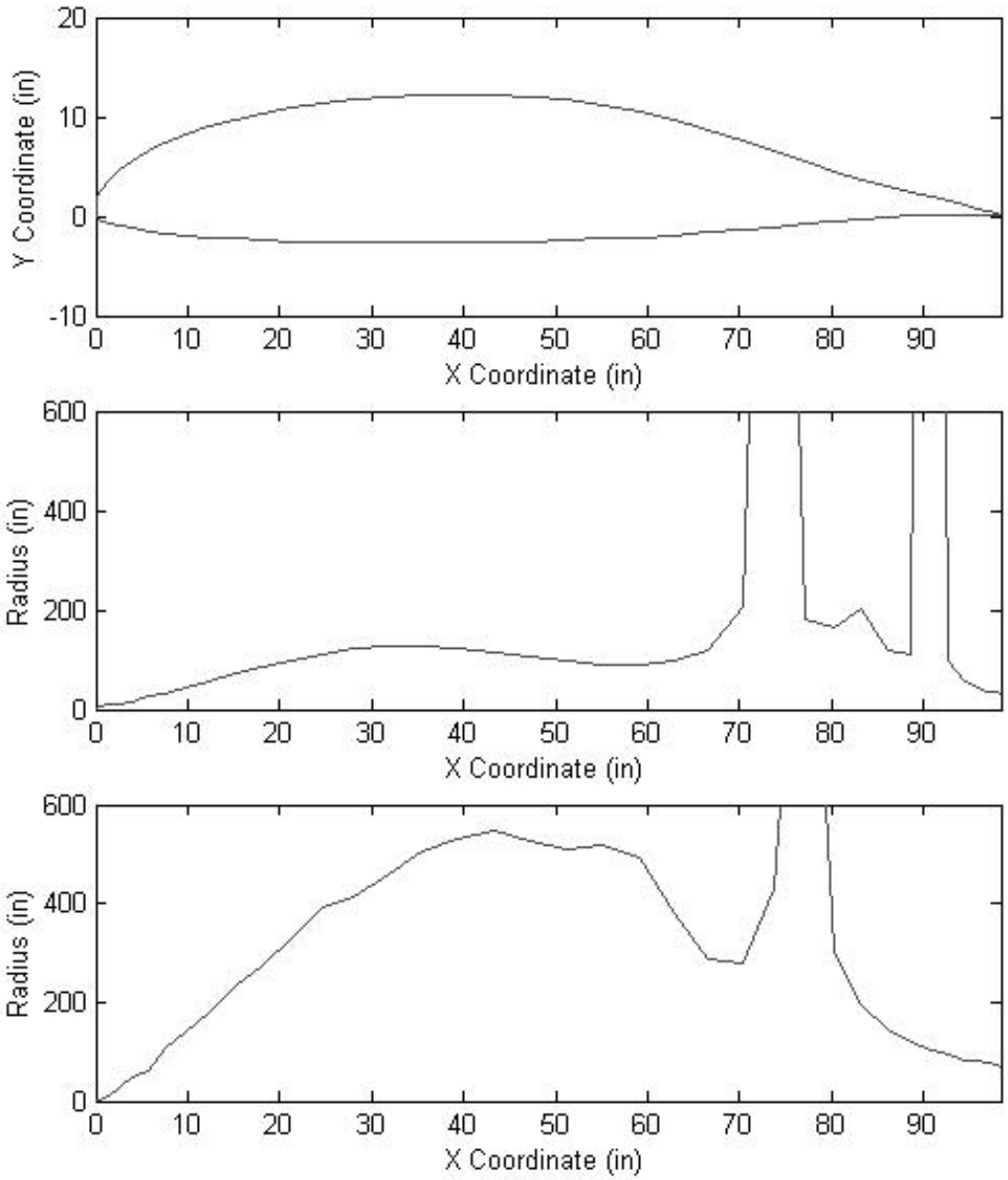

Figure 4.4 Airfoil (top), top surface radius of curvature (middle), and bottom surface radius of curvature (bottom)

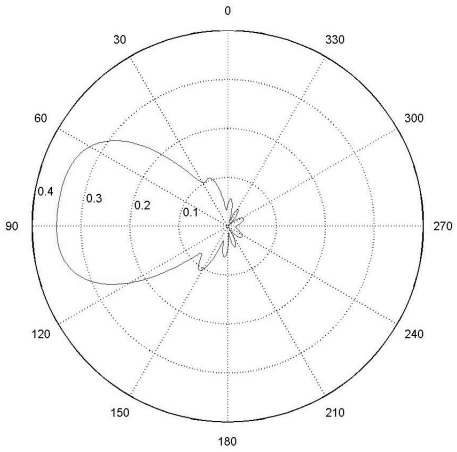

Figure 4.5 Magnitude of $\hat{\phi}$ component of E-field radiation in $\left[\frac{V}{m}\right]$ from 10x40 array on undeformed wing with end-fire phasing: elevation variation ($\phi = 180^o$)

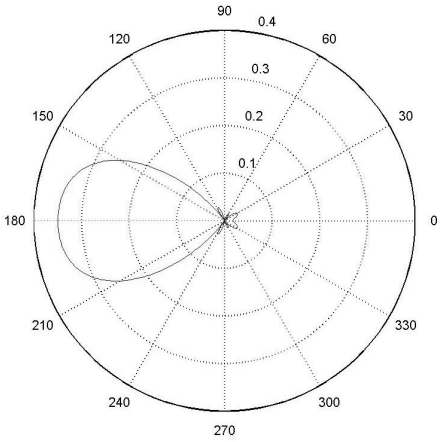

Figure 4.6 Magnitude of $\hat{\phi}$ component of E-field radiation in $\left[\frac{V}{m}\right]$ from 10x40 array on undeformed wing with end-fire phasing: azimuth variation ($\theta = 90^o$)

These plots were generated in MATLAB showed the linear magnitude of the E-field for variations in the elevation angle, θ, and azimuth angle, ϕ. These values were compared to the NEC plots of power gain since the main beam pointing angles should have been the same. The patterns from the NEC-Win Plus+^{TM} analysis are

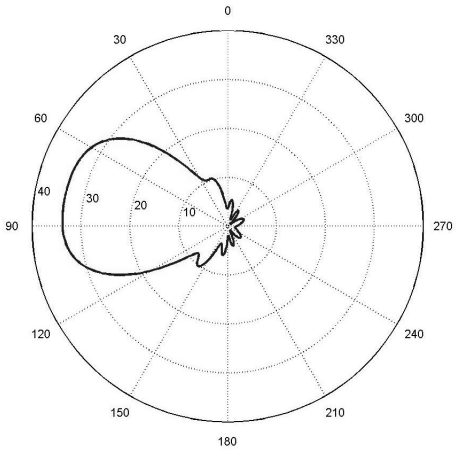

Figure 4.7 Magnitude of $\hat{\phi}$ component of E-field radiation in $\left[\frac{V}{m}\right]$ from 10x40 array for gust load case with end-fire phasing: elevation variation ($\phi = 180^o$)

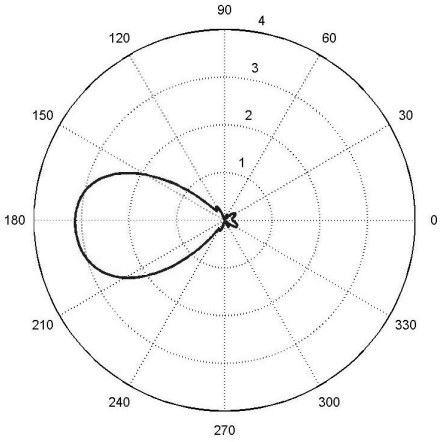

Figure 4.8 Magnitude of $\hat{\phi}$ component of E-field radiation in $\left[\frac{V}{m}\right]$ from 10x40 array for gust load case with end-fire phasing: azimuth variation ($\theta = 90^o$)

shown in Figures 4.9, 4.10, 4.11, and 4.12. The main beam magnitude and angular location are shown in the "Pattern Analysis" box in each figure.

The NEC-Win Plus+^{TM} plots for elevation variation were flipped relative to the plots generated by the MATLAB code. The main beam in both of these plots was still pointing toward $+90^o$, but the perspective changed. The MATLAB code

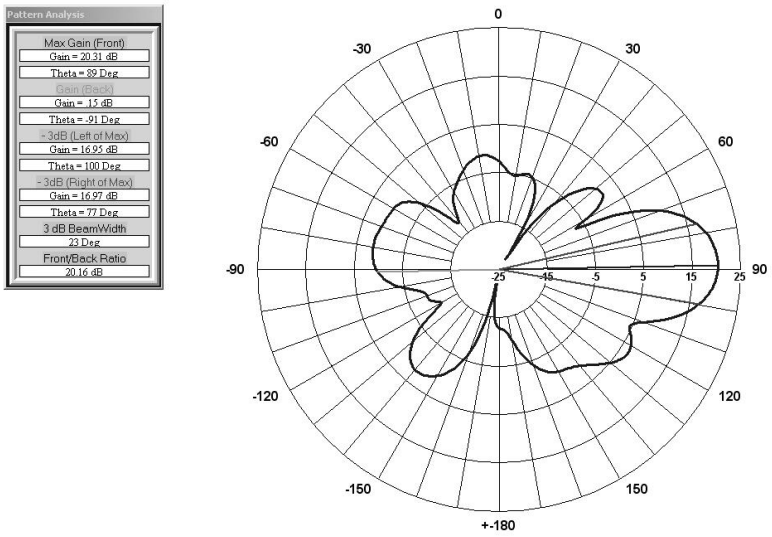

Figure 4.9 NEC-Win Plus+^{TM} plot of gain in dB for the undeformed wing case: elevation variation ($\phi = 180^o$)

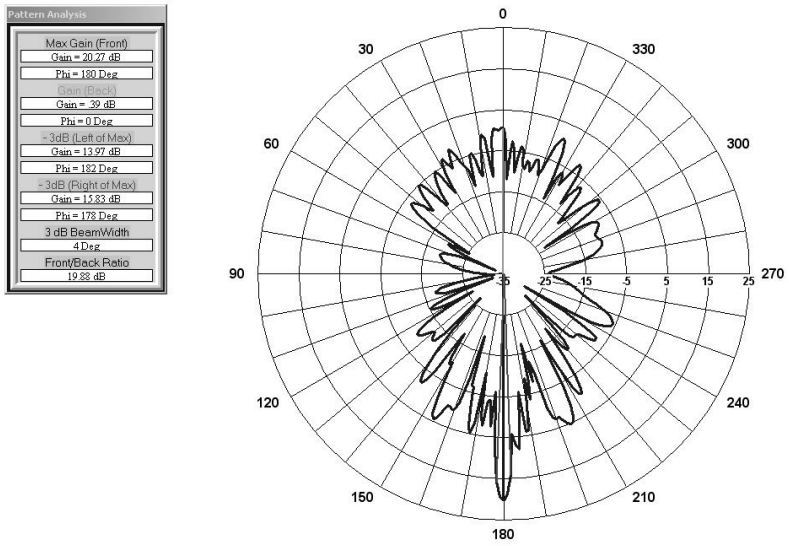

Figure 4.10 NEC-Win Plus+^{TM} plot of gain in dB for the undeformed wing case: azimuth variation ($\theta = 90^o$)

viewpoint is essentially the root of the wing with the beam shooting off to the left, but the NEC viewpoint is from the direction of the tip of the wing. Also, the direction of

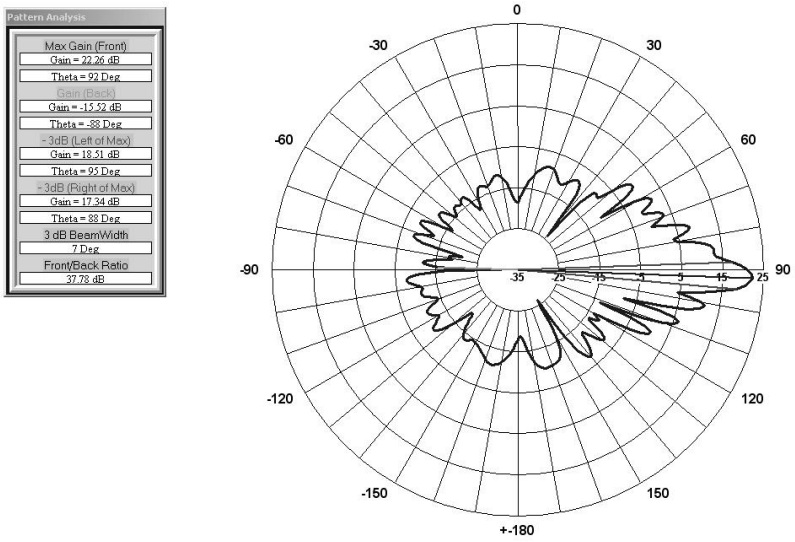

Figure 4.11 NEC-Win Plus+^{TM} plot of gain in units of dB for the gust load deformation case: elevation variation ($\phi = 180^o$)

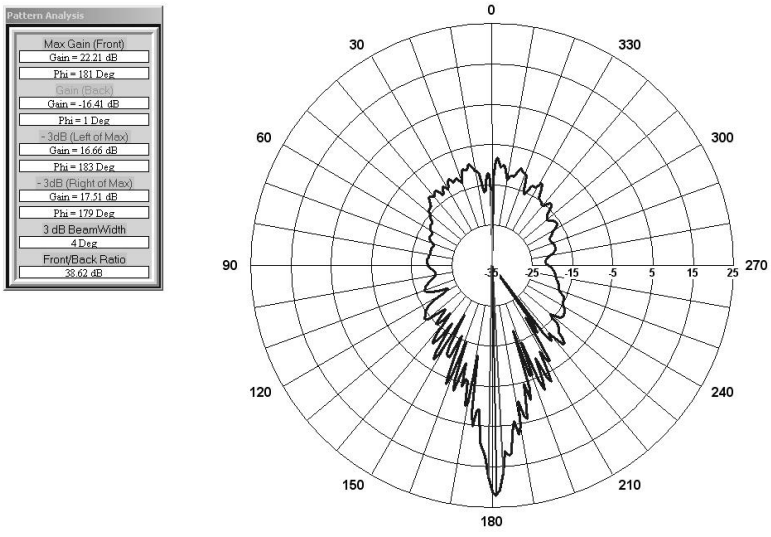

Figure 4.12 NEC-Win Plus+^{TM} plot of gain in units of dB for the gust load deformation case: azimuth variation ($\theta = 90^o$)

180^o in the NEC azimuth plots is downward instead of to the left as is was depicted in the MATLAB plots.

Table 4.1 Comparison of NEC-Win Plus+^{TM} and basic array theory results for angular location and magnitude of E-field maxima for undeformed and gust load cases

TECHNIQUE	LOAD	VARIATION	MAX. ANGLE	MAG. (dB)
Array Theory	Undef Wing	θ	91.1^o	15.301
NEC-Win Plus+^{TM}	Undef Wing	θ	89.0^o	20.31
Array Theory	Undef Wing	ϕ	179.91^o	15.30
NEC-Win Plus+^{TM}	Undef Wing	ϕ	180.0^o	20.27
Array Theory	Gust Load	θ	85.37^o	17.062
NEC-Win Plus+^{TM}	Gust Load	θ	92.0^o	22.26
Array Theory	Gust Load	ϕ	181.05^o	15.29
NEC-Win Plus+^{TM}	Gust Load	ϕ	181.0^o	22.21

The patterns generated by NEC-Win Plus+^{TM} were more refined than the plots generated using basic array theory. The NEC plots show deep nulls separating many grating lobes, but these distinctions are lost when simple field summations are used. The overall patterns show some similarities, but the array theory patterns were wider than the NEC patterns. A comparison of the results generated by the two methods are listed in Table 4.3. These results were generated for a 10x40 element array positioned with the inboard, chordwise edge at the root of the front wing. This was the position of the array when the NEC analysis was performed. One run in NEC-Win Plus+^{TM} took 22.5 hours for a 10x40 element array on a 1.7 GHz Windows PC with 256 MB memory. Also, the cases that were run validated that the MATLAB code was a decent estimation of the numerical solution for the undeformed wing, but it was less reliable for predicting the main beam pointing angle as the wing deflection increased.

The elevation pointing angle calculated by NEC-Win Plus+^{TM} was pitched up 2.1^o compared to the array theory angle for the undeformed wing case, and the magnitude was 5 dB higher. In the azimuth plane the angles were nearly identical, but the magnitudes differed again by 5 dB. For the gust load case, the comparison in elevation angles was opposite the results of the undeformed wing. The array theory

determined that the main beam pitched up almost 6^o compared to the undeformed wing, but NEC-Win Plus+^{TM} found that the beam was actually steered downward 3^o from its undeformed wing result. The azimuth angles were essentially the same once again and the magnitude differences were approximately 5 dB.

4.4 Antenna Results

For the initial antenna analysis, coordinates for the deformed array extending 40 elements in the spanwise direction were derived from a 2.5g steady maneuver load case. The array was located just inboard of the joint section, as was shown in Figure 3.2. This wing loading produced a three-meter vertical deflection at the tip of the wing, but only a one-meter deflection at the outboard edge of the antenna array. When the load case was changed to include a non-linear deflection for a gust load, where the structure was sized for linear analysis, the outboard edge of the array deflected over six meters. The array size was also increased to 60 elements running in the spanwise direction to see if a larger array was more sensitive to the same load configurations. The plots shown in this section are the linear azimuth and elevation plots of the E-field horizontal component magnitude for both of these load cases and for the undeformed wing case.

Figures 4.13 and 4.14 are the undeformed wing array radiation patterns with no phasing applied. As seen in Figure 4.13 for the undeformed wing, curvature of the antenna as it conforms to the airfoil shape in the chordwise direction causes a shift in the pointing direction of the main beam as compared to a planar array. If the airfoil was flattened (z-coordinates set to zero), the theta variation pattern looked like Figure 4.15. For the curved array, the main beam shifts clockwise approximately seven degrees.

The large grating lobe that appears opposite the main beam in these figures was expected unless phasing was applied that steered the main beam to end-fire, and the interelement spacing was considerably less than half a wavelength. It was discovered

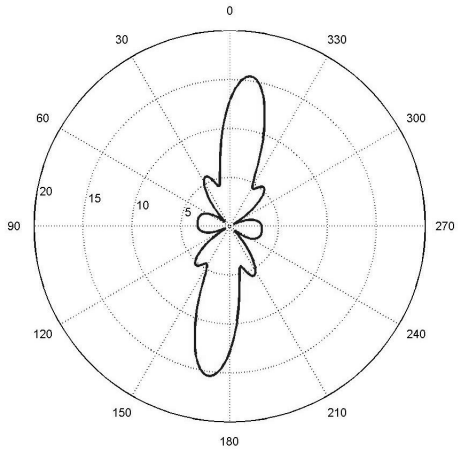

Figure 4.13 Magnitude of $\hat{\phi}$ component of E-field radiation in $\left[\frac{V}{m}\right]$ from 5x40 array on undeformed wing with zero phasing: elevation variation ($\phi = 180^o$)

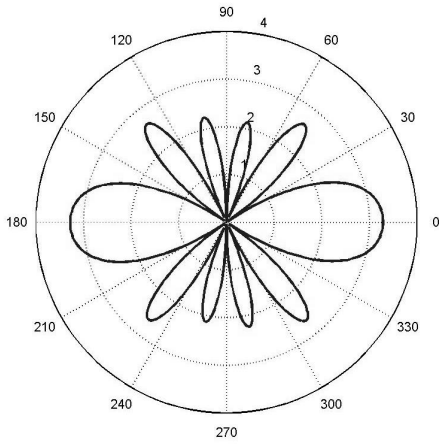

Figure 4.14 Magnitude of $\hat{\phi}$ component of E-field radiation in $\left[\frac{V}{m}\right]$ from 5x40 array on undeformed wing with zero phasing: azimuth variation ($\theta = 90^o$)

that simply changing the phasing to an end-fire configuration did not eliminate the grating lobe. Therefore the number of dipoles used in generating these plots was increased from 5 to 10 for the same array chord length. This was done because the spacing for five dipoles was approximately half a wavelength. The actual, conformal elements are intended to have only one main beam and no large grating lobes. The

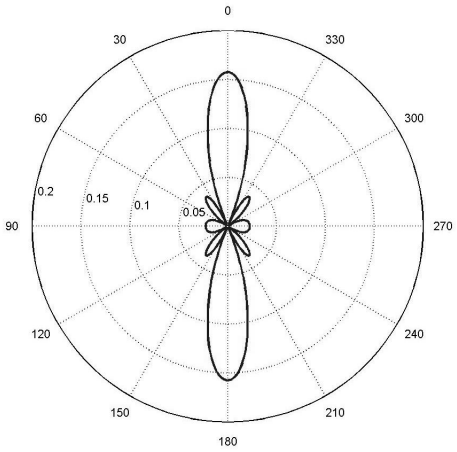

Figure 4.15 Magnitude of $\hat{\phi}$ component of E-field radiation in $\left[\frac{V}{m}\right]$ from 5x40 array on flattened airfoil with zero phasing: elevation variation ($\phi = 180^o$)

CLAS elements accomplish this due to their geometry, but very thin dipoles at the same center point locations do not. Increasing the number of dipoles to 10 corresponds to roughly a quarter wavelength spacing for a frequency of 430 MHz. Figures 4.16, 4.17, and 4.18 show the undeformed array Great Circle pattern cuts of a 10x40 element array with phasing applied to steer the beam to an end-fire configuration and a smaller interelement spacing. The extremely small magnitude of the radiated field in Figure 4.18 was a common to all the load cases, and therefore only one plot is presented for this pattern cut, which pertains to an elevation, θ, variation with $\phi = 90^o$.

The effects of typical wing deformation on the 10x40 array pointing accuracy proved to be significant for the 2.5g steady load case, and even more so for the gust load case. The radiation patterns for this case are shown in Figures 4.19, 4.20, 4.21, and 4.22.

While the differences are hard to see on these plots, the angular location of the maxima changed considerably. The undeformed, 2.5g load, and gust load radiation patterns for elevation, θ, and azimuth, ϕ, variations are shown in Table 4.4,

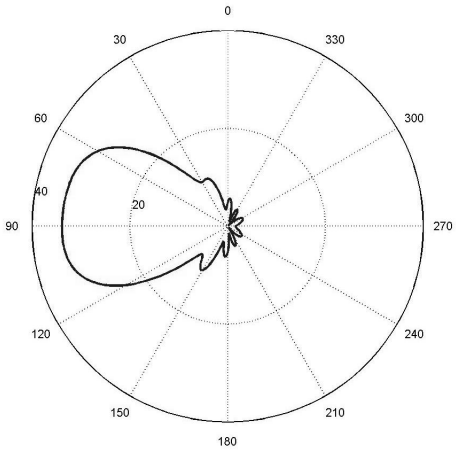

Figure 4.16 Magnitude of $\hat{\phi}$ component of E-field radiation in $\left[\frac{V}{m}\right]$ from 10x40 array on undeformed wing with end-fire phasing: elevation variation ($\phi = 180^o$)

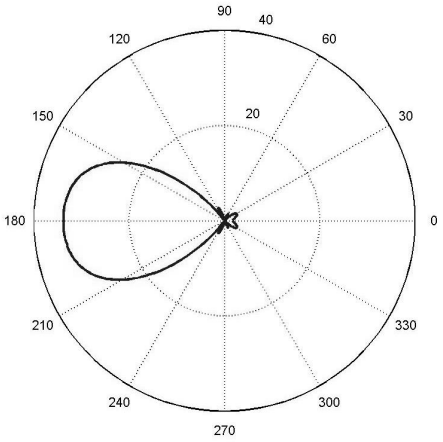

Figure 4.17 Magnitude of $\hat{\phi}$ component of E-field radiation in $\left[\frac{V}{m}\right]$ from 10x40 array on undeformed wing with end-fire phasing: azimuth variation ($\theta = 90^o$)

which lists the angular location of the maxima, linear magnitudes in units of $\frac{V}{m}$, and magnitudes in dB.

Considering the undeformed wing case as the baseline, the maximum value of the E-field magnitude for the elevation plots remained virtually the same when the

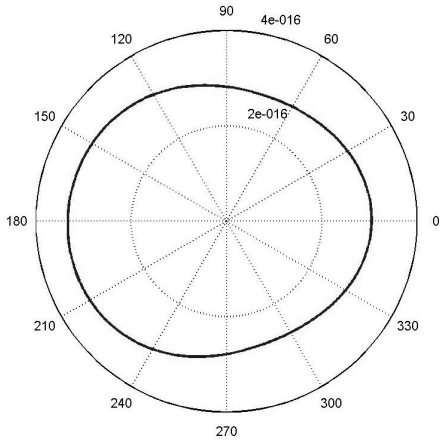

Figure 4.18 Magnitude of $\hat{\phi}$ component of E-field radiation in $\left[\frac{V}{m}\right]$ from 10x40 array on undeformed wing with end-fire phasing: elevation variation ($\phi = 90^o$)

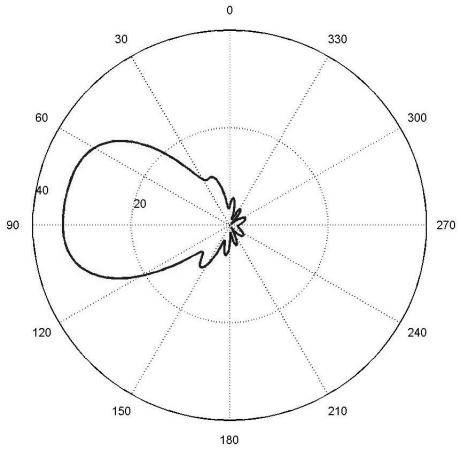

Figure 4.19 Magnitude of $\hat{\phi}$ component of E-field radiation in $\left[\frac{V}{m}\right]$ from 10x40 array for 2.5g load case with end-fire phasing: elevation variation ($\phi = 180^o$)

2.5g load was applied, but it decreased by 0.031 $\frac{V}{m}$ for the gust load case. In the azimuth plots, the maximum value increased by 0.002 $\frac{V}{m}$ for the 2.5g load, but the magnitude for the gust load decreased by 0.159 $\frac{V}{m}$. The angular location of the E-field elevation maximum magnitude decreased for both cases of applied loads. The

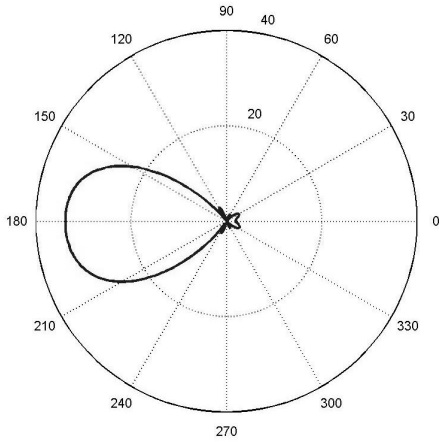

Figure 4.20 Magnitude of $\hat{\phi}$ component of E-field radiation in $\left[\frac{V}{m}\right]$ from 10x40 array for 2.5g load case with end-fire phasing: azimuth variation ($\theta = 90^o$)

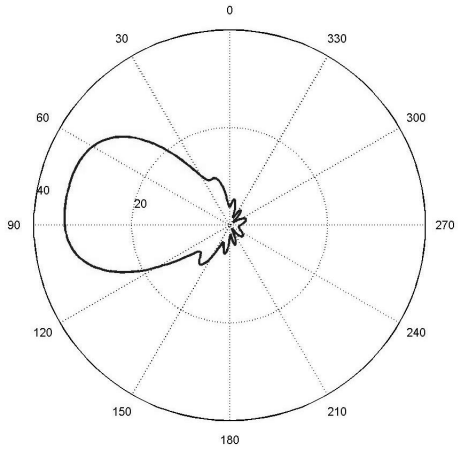

Figure 4.21 Magnitude of $\hat{\phi}$ component of E-field radiation in $\left[\frac{V}{m}\right]$ from 10x40 array for gust load case with end-fire phasing: elevation variation ($\phi = 180^o$)

gust load case was the most severe of the two loads, and caused the main beam to shift up 9.17^o. In the azimuth plots, the 2.5g load caused no shift in the pointing angle, but the gust load caused the main beam to shift to the left 1.72^o.

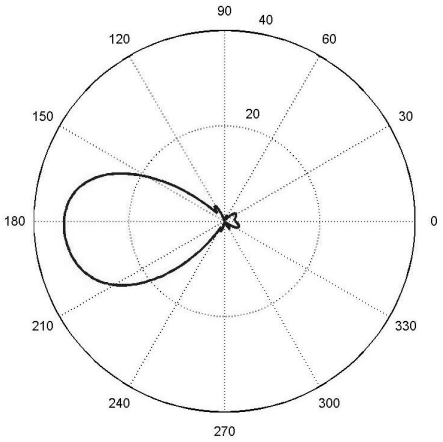

Figure 4.22 Magnitude of $\hat{\phi}$ component of E-field radiation in $\left[\frac{V}{m}\right]$ from 10x40 array for gust load case with end-fire phasing: azimuth variation ($\theta = 90^o$)

Table 4.2 Angular location and magnitude of front wing 10x40 element array E-field maxima for undeformed, 2.5g load, and gust load cases

LOAD CASE	VARIATION	MAX. ANGLE	MAG. $\left(\frac{V}{m}\right)$	MAG. (dB)
Undeformed Wing	θ	92.25^o	33.890	15.301
2.5g Maneuver Load	θ	88.55^o	33.888	15.30
Gust Load	θ	81.80^o	33.857	15.297
Undeformed Wing	ϕ	179.91^o	33.880	15.30
2.5g Maneuver Load	ϕ	179.91^o	33.882	15.30
Gust Load	ϕ	181.63^o	32.723	15.279

The array was lengthened to 60 elements in the spanwise direction to see if a longer array would have more noticeable degradation in pointing accuracy due to wing deformation. The radiation pattern cuts from the 10x60 element array on an undeformed wing are shown in Figures 4.23 and 4.24. The results are shown in Table 4.4.

Again considering the undeformed wing case as the baseline, the maximum value of the E-field magnitude for the elevation plots decreased by only 0.006 $\frac{V}{m}$ when the 2.5g load was applied, but it decreased by 0.085 $\frac{V}{m}$ for the gust load case.

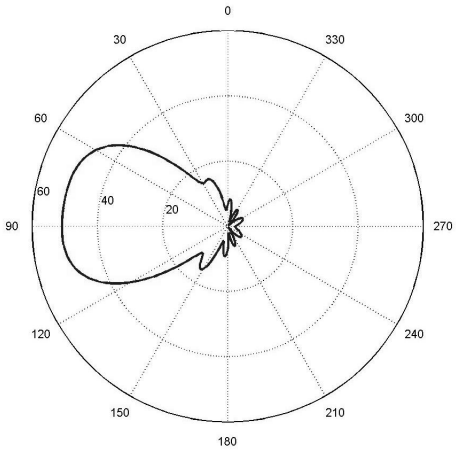

Figure 4.23 Magnitude of $\hat{\phi}$ component of E-field radiation in $\left[\frac{V}{m}\right]$ from 10x60 array on undeformed wing with end-fire phasing: elevation variation ($\phi = 180^o$)

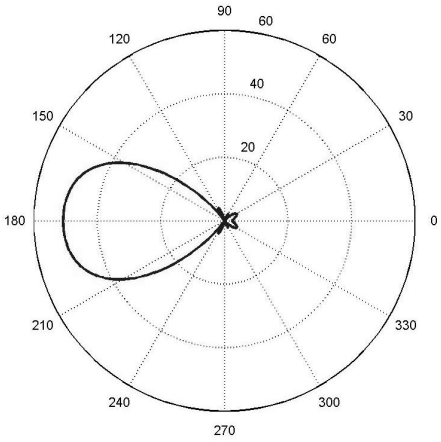

Figure 4.24 Magnitude of $\hat{\phi}$ component of E-field radiation in $\left[\frac{V}{m}\right]$ from 10x60 array on undeformed wing with end-fire phasing: azimuth variation ($\theta = 90^o$)

In the azimuth plots, the maximum value decreased by 0.025 $\frac{V}{m}$ for the 2.5g load, and the magnitude for the gust load decreased by 0.286 $\frac{V}{m}$. The angular location of the E-field elevation maximum magnitude once again decreased for both cases of applied loads. The gust load case caused the main beam to shift up 8.02^o. For the

Table 4.3 Angular location and magnitude of front wing 10x60 element array E-field maxima for undeformed, 2.5g load, and gust load cases

LOAD CASE	VARIATION	MAX. ANGLE	MAG. $\left(\frac{V}{m}\right)$	MAG. (dB)
Undeformed Wing	θ	90.53^o	50.839	17.062
2.5g Maneuver Load	θ	87.40^o	50.833	17.061
Gust Load	θ	81.23^o	50.754	17.055
Undeformed Wing	ϕ	179.91^o	50.837	17.062
2.5g Maneuver Load	ϕ	180.48^o	50.812	17.060
Gust Load	ϕ	182.20^o	50.551	17.037

azimuth plots, the 2.5g load caused a 0.57^o shift in the pointing angle, and the gust load caused the main beam to shift to the left 2.29^o.

A 10x60 element array was placed on the aft wing. The radiation pattern cuts from the array on an undeformed wing are shown in Figures 4.25 and 4.26. The patterns due to the 2.5g maneuver load are shown in Figures 4.27 and 4.28, and for the gust load the linear E-field plots are shown in Figures 4.29 and 4.30 The results are shown in Table 4.4.

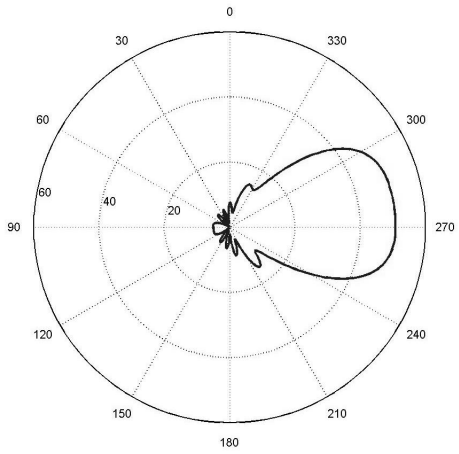

Figure 4.25 Magnitude of $\hat{\phi}$ component of E-field radiation in $\left[\frac{V}{m}\right]$ from 10x60 array on undeformed aft wing with end-fire phasing: elevation variation ($\phi = 180^o$)

Deviation from the undeformed wing case showed that the maximum value of the E-field magnitude for the elevation plots decreased by only 0.005 $\frac{V}{m}$ when the

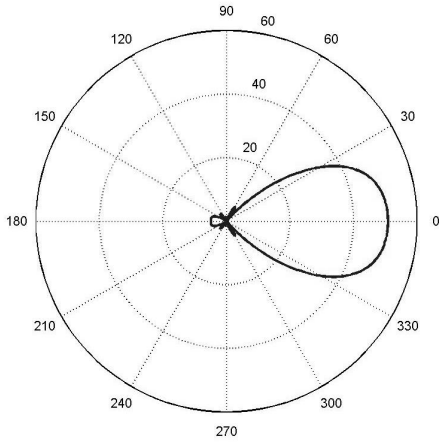

Figure 4.26 Magnitude of $\hat{\phi}$ component of E-field radiation in $\left[\frac{V}{m}\right]$ from 10x60 array on undeformed aft wing with end-fire phasing: azimuth variation ($\theta = 90^o$)

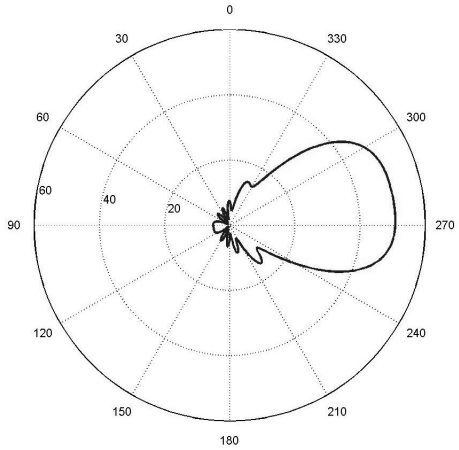

Figure 4.27 Magnitude of $\hat{\phi}$ component of E-field radiation in $\left[\frac{V}{m}\right]$ from 10x60 array on aft wing for 2.5g load case with end-fire phasing: elevation variation ($\phi = 180^o$)

2.5g load was applied, and it decreased by 0.009 $\frac{V}{m}$ for the gust load case. So there was essentially no change in magnitude. In the azimuth plots, the maximum value decreased by 0.035 $\frac{V}{m}$ for the 2.5g load, and the magnitude for the gust load decreased by 0.146 $\frac{V}{m}$. The angular location of the E-field elevation maximum magnitude

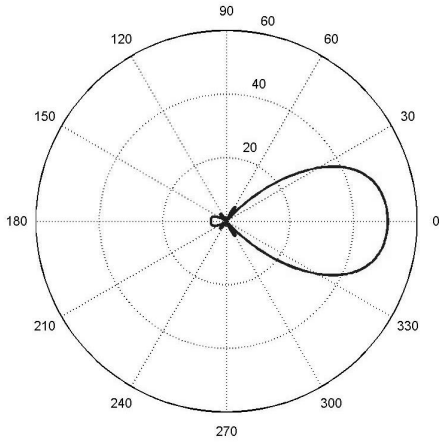

Figure 4.28 Magnitude of $\hat{\phi}$ component of E-field radiation in $\left[\frac{V}{m}\right]$ from 10x60 array on aft wing for 2.5g load case with end-fire phasing: azimuth variation ($\theta = 90^o$)

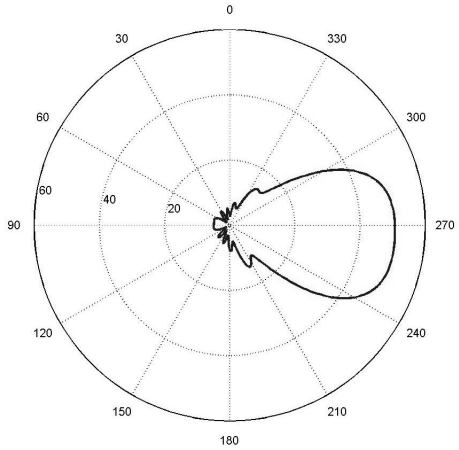

Figure 4.29 Magnitude of $\hat{\phi}$ component of E-field radiation in $\left[\frac{V}{m}\right]$ from 10x60 array on aft wing for gust load case with end-fire phasing: elevation variation ($\phi = 180^o$)

decreased for both cases of applied loads. The gust load case caused the main beam to shift up 9.14^o. For the azimuth plots, the pointing angle remained virtually unchanged.

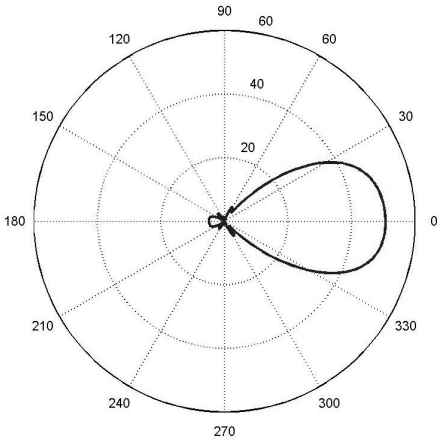

Figure 4.30 Magnitude of $\hat{\phi}$ component of E-field radiation in $\left[\frac{V}{m}\right]$ from 10x60 array on aft wing for gust load case with end-fire phasing: azimuth variation ($\theta = 90^o$)

Table 4.4 Angular location and magnitude of aft wing 10x60 element array E-field maxima for undeformed, 2.5g load, and gust load cases

LOAD CASE	VARIATION	MAX. ANGLE	MAG. $\left(\frac{V}{m}\right)$	MAG. (dB)
Undeformed Wing	θ	271.0^o	50.851	17.063
2.5g Maneuver Load	θ	273.87^o	50.846	17.063
Gust Load	θ	261.84^o	50.842	17.061
Undeformed Wing	ϕ	0.0^o	50.847	17.063
2.5g Maneuver Load	ϕ	0.0^o	50.812	17.060
Gust Load	ϕ	359.82^o	50.701	17.050

Increasing the size of the array caused the magnitude of the electromagnetic field to be greater, but the magnitude was slightly more sensitive to deformation than it was for the shorter array. Comparing the pointing accuracy of the two arrays showed that the larger array had a slight advantage in the elevation variation, but its main beam experienced a larger shift in the azimuth plane. Neither array was able to maintain the desired end-fire pointing configuration of $\theta = 90^o$ and $\phi = 180^o$.

4.5 Aileron Effectiveness

The control surface was found to be only 5% effective in generating lift to trim the aircraft in pitch. This confirmed that an inboard control surface or aft wing twist ought to be used to trim this aircraft for level amneuvers. The roll effectiveness of the aileron was also evaluated for various Mach numbers. At the intended loiter Mach number of 0.6 (V = 204.17 $\frac{m}{s}$), the non-dimensional roll rate was found to be slightly negative ($p = -5.01x10^{-4}$), which meant that aileron reversal had occurred. The dynamic pressure was varied slightly to bracket the reversal speed. At a velocity of 203.64 $\frac{m}{s}$ the non-dimensional roll rate was positive ($p = 3.31x10^{-4}$), which meant that the aileron was rolling the aircraft in the intended direction.

V. Conclusion

This study shows that the radiation patterns of an arrays that conform to the surface of the front and aft wing sections of the joined wing undergo significant distortion due to typical wing deflections. For a highly deformed wing due to a gust load, simple phasing of the array was not adequate to keep the beam pointed in the desired direction. Even for a steady 2.5g maneuver load, the change in the main beam elevation angle was substantial. Active control by sensing wing deformations may help compensate for some of the error in beam steering, but structural modifications may also be necessary for the configuration described in this effort.

Comparison of the patterns with a Method of Moments solution showed a 6.6^o degree difference in the main beam elevation angle for a gust load, but only a 2^o difference for the undeformed wing case. The azimuth angles for all of the load cases were essentially the same. The MATLAB code can be easily incorporated into an aircraft design environment where a structural engineer can use this information to design aircraft around a large sensor suite such as the one presented in this effort. The NEC-Win Plus+^{TM} software would be impossible to incorporate into the AVTIE environment because each source has to be placed and configured manually. Therefore, the method presented provides a quick and reasonable estimation of the conformal array radiation pattern of an array placed anywhere on the undeformed wing, but it is less reliable as the wing deflection increases.

A control surface on the wing tip section of this joined wing was not effective for rolling the aircraft, because roll reversal occurs just before Mach 0.6 at sea level conditions. The aileron was also not effective for pitching the aircraft. Therefore, aft wing twist was justified to trim the aircraft for pitch.

5.1 Future Research

There are several areas of this research that were either not attempted due to time constraints or need further development. These topics are listed below:

1. Increase the fidelity of the current finite element composite model for a more exact design.
2. Look at a vertical dipole or some other element (square-loop, patch, etc.).
3. Model the actual antenna elements or incorporate contractor data into the methodology presented here.
4. Place sensor arrays on the bottom surfaces of both the front and aft wing sections inboard of the joint, and couple top and bottom arrays together
5. Look at a smaller, high frequency antenna out on the tip section of the wing.
6. Optimize the various configurations of the antenna arrays and control surfaces.

Appendix A. LRN-1015 Data Points

UPPER			LOWER	
X	Z		X	Z
0	0		0	0
0.001621	0.01707		0.001621	-0.001976
0.006475	0.026197		0.006475	-0.00493
0.014529	0.036312		0.014529	-0.007513
0.025732	0.04699		0.025732	-0.01001
0.04001	0.057142		0.04001	-0.012525
0.057272	0.066677		0.057272	-0.014983
0.077405	0.075746		0.077405	-0.017226
0.100279	0.084202		0.100279	-0.019318
0.125745	0.092004		0.125745	-0.021214
0.153638	0.099088		0.153638	-0.022877
0.183777	0.105433		0.183777	-0.024304
0.215968	0.110974		0.215968	-0.025466
0.25	0.115663		0.25	-0.026357
0.285654	0.119458		0.285654	-0.026977
0.322698	0.122299		0.322698	-0.027302
0.360891	0.124114		0.360891	-0.02733
0.399987	0.124809		0.399987	-0.027065
0.439732	0.124264		0.439732	-0.026505
0.479867	0.122351		0.479867	-0.025652

continued on next page ...

0.520133	0.118919		0.520133	-0.024494
0.560268	0.113813		0.560268	-0.023028
0.600013	0.106947		0.600013	-0.021274
0.639109	0.098407		0.639109	-0.019239
0.677302	0.088455		0.677302	-0.016865
0.714346	0.077492		0.714346	-0.014081
0.75	0.06623		0.75	-0.010938
0.784032	0.055549		0.784032	-0.007663
0.816223	0.046102		0.816223	-0.004646
0.846362	0.037889		0.846362	-0.00213
0.874255	0.030724		0.874255	-0.000215
0.899721	0.024801		0.899721	0.001069
0.922595	0.020019		0.922595	0.001761
0.942728	0.015794		0.942728	0.001957
0.95999	0.01182		0.95999	0.001792
0.974268	0.008107		0.974268	0.001378
0.985471	0.004834		0.985471	0.000884
0.993525	0.002244		0.993525	0.000429
0.998379	0.000577		0.998379	0.000113
1	0		1	0

Appendix B. THE FOURIER TRANSFORM

This information was adapted from Dr. Andrew Terzuoli's *Antennas I* class notes.

Take two arbitrary 1-D spaces $\vec{W}$ and $\vec{S}$, where W and S are real variables such that their product (WS) is unitless. These spaces are called inverse spaces, with complex functions $\underline{f}(W)$, $\underline{F}(S)$ that can be related by the Fourier Transform given by:

$$\begin{aligned} \underline{f}\,(W) &= \int_{-\infty}^{\infty} \underline{F}\,(S)\, e^{j2\pi(WS)} dS \\ \underline{F}\,(S) &= \int_{-\infty}^{\infty} \underline{f}\,(W)\, e^{-j2\pi(WS)} dW \end{aligned}$$

Now apply to radiation and scattering by a current, where

$$\bar{\underline{\mathrm{J}}}_R\,(\theta,\phi,\omega) = \int_{|\vec{r}'|} \underline{\bar{J}}_R\,(\vec{r}',\omega)\, e^{\underline{\gamma}(\omega)\vec{r}'\cdot\hat{r}(\theta,\phi)} d\,|\vec{r}'|$$

and

$$\underline{\bar{A}}_R(\bar{r}_s,\omega) = \underline{\mu}(\omega)\underline{\Psi}(r,\omega)\underline{\bar{J}}_R(\theta,\phi,\omega).$$

In these equations, $\underline{\gamma} = \alpha + j\beta$, where α is the attenuation and β is the propagation of the radiation, and

$$\underline{\Psi} = \frac{e^{-\underline{\gamma}r}}{4\pi r}.$$

An engineering approximation is made here that ignores the transverse attenuation in the integral. Therefore, in the integral there is only transverse resonance and $\underline{\gamma} = j\beta$. Then

$$\bar{\underline{\mathrm{J}}}_R\,(\theta,\phi,\omega) = \int_{|\vec{r}'|} \underline{\bar{J}}_R\,(\vec{r}',\omega)\, e^{j\beta(\omega)\vec{r}'\cdot\hat{r}(\theta,\phi)} d\,|\vec{r}'|$$

where $j\beta(\omega)\vec{r}'\cdot\hat{r}(\theta,\phi)$ is a real number.

The source is now restricted to rectangular variables, thus let

$$\vec{r}'_R = x'\hat{x} + y'\hat{y} + z'\hat{z}$$

and the dot product, $\vec{r}'_R \cdot \hat{r}$, becomes

$$\vec{r}'_R \cdot \hat{r} = x'(\hat{x} \cdot \hat{r}) + y'(\hat{y} \cdot \hat{r}) + z'(\hat{z} \cdot \hat{r})$$

where the dot products of this equation are the direction cosines:

$$\begin{aligned} (\hat{x} \cdot \hat{r}) &= \cos\theta_x \\ (\hat{y} \cdot \hat{r}) &= \cos\theta_y \\ (\hat{z} \cdot \hat{r}) &= \cos\theta_z. \end{aligned}$$

If now transformed to spherical coordinates, the direction cosines become

$$\begin{aligned} \cos\theta_x &= \sin\theta\cos\phi \\ \cos\theta_y &= \sin\theta\sin\phi \\ \cos\theta_z &= \cos\theta. \end{aligned}$$

Then defining

$$\begin{aligned} \beta_x &\hat{=} \beta\cos\theta_x \\ \beta_y &\hat{=} \beta\cos\theta_y \\ \beta_z &\hat{=} \beta\cos\theta_z \end{aligned}$$

β times the vector dot product becomes

$$\beta(\vec{r}'_R \cdot \hat{r}) = x'\beta_x + y'\beta_y + z'\beta_z = \vec{r}'_R \cdot \vec{\beta}_R(\theta, \phi, \omega).$$

This real, unitless dot product is substituted back into the integral to give

$$\bar{\underline{J}}_R(\theta, \phi, \omega) = \int_{|\vec{r}'|} \bar{\underline{J}}_R(\vec{r}', \omega)\, e^{j\vec{\beta}_R \cdot \vec{r}'_R} d\,|\vec{r}'|$$

which is a three-dimensional Fourier Transform.

Vita

Captain Ben P. Smallwood graduated from Prattsburgh Central School in Prattsburgh, New York, in June 1994. He entered undergraduate studies at Clarkson University in Potsdam, New York, where he graduated with a Bachelor of Science Degree in Aeronautical Engineering and earned an ROTC commission in May 1998.

His first assignment was as a digital simulation specialist at the Air Force Research Laboratory's Munitions Directorate, Eglin AFB, Florida. He managed several programs for the Advanced Guidance and Simulation Branch, which included development of a High Frequency Motion Simulator and a Target Simulator Optical System for the Kinetic Kill Vehicle Hardware-in-the-Loop Simulation Facility. In August 2001, he entered the Graduate School of Engineering, Air Force Institute of Technology, to study Aeronautical Engineering. Upon graduation, he will be assigned to the Air Force Research Laboratory, Sensors Directorate at Wright-Patterson AFB, Ohio.

Bibliography

1. Balanis, C. A. *Antenna Theory: Analysis and Design*. John Wiley & Sons, Inc., 1997.

2. Blair, M. and R. A. Canfield. "A Joined-Wing Structural Weight Modeling Study." 43^{rd} *AIAA/ASME/ASCE/AHS/ASC Structures, Structural Dynamics and Materials Conference, Denver, CO*. Number AIAA 2002-1337. April 2002.

3. Gallman, J. W. and I. M. Kroo. "Structural Optimization for Joined-Wing Synthesis," *Journal of Aircraft*, *33*(1) (January and February 1996).

4. Hexcel Composites, "$HexWeb^{TM}$ Honeycomb Attributes and Properties." http://www.hexcelcomposites.com/Markets/Products/Honeycomb/Hexweb_attrib/hw_p08.htm.

5. Kummer, W. H. "Basic Array Theory," *Proceedings of the IEEE*, *80*(1) (January 1992).

6. Lin, H-H, et al. "Influence of Joint Fixity on the Aeroelastic Characteristics of a Joined Wing Structure." 31^{st} *AIAA/ASME/ASCE/AHS/ASC Structures, Structural Dynamics and Materials Conference, Long Beach, CA*. 1442–1454. April 1990.

7. Livne, E. "Aeroelasticity of Joined-Wing Airplane Configurations: Past Work and Future Challenges - A Survey." 42^{nd} *AIAA/ASME/ASCE/AHS/ASC Structures, Structural Dynamics and Materials Conference, Seattle, WA*. Number AIAA 2001-1370. April 2001.

8. MacNeal-Schwendler Corporation. *MSC.NASTRAN Version 68 Reference Manual*, 1995.

9. Mailloux, R. J. "Conformal and low-profile arrays." *Antenna Engineering Handbook* chapter 21, 1–21, McGraw-Hill, 1981.

10. The MathWorks, Inc. *MATLAB Reference Guide: Version 6.1*, 2001.

11. MSC.Software Corporation. *MSC.FlightLoads and Dynamics User's Guide Version 2001 (r2)*, 2001.

12. Neill, D. J., et al. "ASTROS - A Multidisciplinary Automated Structural Design Tool," *Journal of Aircraft*, *27*(12):1021–1027 (1990).

13. Nittany Scientific, Inc., "NEC-2 User's Guide." http://www.nittany-scientific.com/nec.

14. Nittany Scientific, Inc. *NEC-Win Plus+^{TM} Reference and User's Manual: Antenna Analysis Software Version 1.1*, November 1999.

15. Northrop Grumman Corporation. *SensorCraft Low Band Conformal Load Bearing Antenna Structures (S-CLAS): R & D Status Report No. 13*. Contract F33615-00-D-3054, 0005, August 2002.

16. Public Domain Aeronautical Software. *User's Guide-PAN AIR Technology Program for Solving Potential Flow about Arbitrary Configurations*, 1992.

17. Reich, G. W., et al. "Application of Active Aeroelastic Wing Technology to a Joined-Wing Sensorcraft." 43^{rd} *AIAA/ASME/ASCE/AHS/ASC Structures, Structural Dynamics and Materials Conference, Denver, CO*. Number AIAA 2002-1633. April 2002.

18. Roberts, Capt Ronald W. *Sensor-Craft Analytical Certification*. MS thesis, AFIT/GAE/ENY/03M-6, Graduate School of Engineering, Air Force Institute of Technology (AETC), Wright-Patterson AFB OH, March 2003.

19. Smith, S. C., et al. "The Design of a Joined-Wing Flight Demonstrator Aircraft." *Proceedings of the AIAA/AHS/ASEE Aircraft Design, Systems and Operations Meeting, St. Louis, MO*. Number AIAA 1987-2930. September 1987.

20. Structural Dynamics Research Corporation. *I-DEAS Student Guide*, 1999.

21. Stutzman, W. L. and G. A. Thiele. *Antenna Theory and Design*. Wiley, 1981.

22. TechnoSoft Inc. *Adaptive Modeling Language Basic Training Manual: Version 2.07*, 2001.

23. Wolkovitch, J. "Joined Wing Aircraft," *US Patent*, (#3,942,747) (March 1976).

24. Wolkovitch, J. "Joined Wing Aircraft," *US Patent*, (#4,365,773) (December 1982).

25. Wolkovitch, J. "The Joined Wing: An Overview," *Journal of Aircraft*, *23*:161–178 (March 1986).

REPORT DOCUMENTATION PAGE

Form Approved
OMB No. 0704–0188

1. REPORT DATE *(DD–MM–YYYY)*	2. REPORT TYPE	3. DATES COVERED *(From — To)*
25–03–2003	Master's Thesis	Sep 2001 — Mar 2003

4. TITLE AND SUBTITLE

STRUCTURALLY INTEGRATED ANTENNAS ON A JOINED-WING AIRCRAFT

5a. CONTRACT NUMBER

5b. GRANT NUMBER

5c. PROGRAM ELEMENT NUMBER

6. AUTHOR(S)

Smallwood, Ben P., Captain, USAF

5d. PROJECT NUMBER

5e. TASK NUMBER

5f. WORK UNIT NUMBER

7. PERFORMING ORGANIZATION NAME(S) AND ADDRESS(ES)

Air Force Institute of Technology
Graduate School of Engineering and Management
2950 Hobson Way, Building 640
WPAFB OH 45433-7765

8. PERFORMING ORGANIZATION REPORT NUMBER

AFIT/GAE/ENY/03-7

9. SPONSORING / MONITORING AGENCY NAME(S) AND ADDRESS(ES)

AFRL/VA
2210 Eighth Street, Rm. 220
Wright Patterson AFB OH 45433
937-255-8430
Dr. Maxwell Blair

DAGSI
3155 Research Blvd., Ste 205
Kettering, OH 45420
937-781-4000
Dr. Elizabeth Downie

10. SPONSOR/MONITOR'S ACRONYM(S)

11. SPONSOR/MONITOR'S REPORT NUMBER(S)

12. DISTRIBUTION / AVAILABILITY STATEMENT

APPROVAL FOR PUBLIC RELEASE; DISTRIBUTION IS UNLIMITED.

13. SUPPLEMENTARY NOTES

14. ABSTRACT

This research is a foundational study of conformal, load-bearing antenna arrays embedded into the wing structure of a joined-wing aircraft. The antenna performance, Finite Element Model (FEM), and control surface effectiveness are investigated. The theory describing an ensemble of dipole antenna elements that conform to the shape of a section of the joined wing is developed. The far field, free space radiation pattern of the sensor is then analyzed for a wing that is deflected due to typical aerodynamic loading and compared to the undeformed wing array. A FEM of the antenna elements is created and incorporated into the full FEM of the joined-wing aircraft allowing its structural impact to be realized. Based on the positioning of these large sensor arrays, control surfaces are placed and examined to achieve the proper handling capabilities necessary for this type of aircraft. The results of this study show that wing deflections due to typical aerodynamic loads produce significant disturbances to the radiation pattern of a conformal antenna when end-fire phasing is applied.

15. SUBJECT TERMS

conformal antenna array; joined-wing aircraft

16. SECURITY CLASSIFICATION OF:			17. LIMITATION OF ABSTRACT	18. NUMBER OF PAGES	19a. NAME OF RESPONSIBLE PERSON
a. REPORT	b. ABSTRACT	c. THIS PAGE			Robert A. Canfield, LtCol, ENY
U	U	U	UU	89	19b. TELEPHONE NUMBER *(include area code)* (937) 255–3636, ext 4641